Characteristics of ice-structure-soil interaction of an offshore wind turbine

Zou, Pengxu; Bricker, Jeremy D.; Fujisaki-Manome, Ayumi; Garcia, Fernando E.

DOI
10.1016/j.oceaneng.2024.116975

Publication date
2024

Document Version
Final published version

Published in
Ocean Engineering

Citation (APA)
Zou, P., Bricker, J. D., Fujisaki-Manome, A., & Garcia, F. E. (2024). Characteristics of ice-structure-soil interaction of an offshore wind turbine. *Ocean Engineering*, *295*, Article 116975. https://doi.org/10.1016/j.oceaneng.2024.116975

Ocean Engineering 295 (2024) 116975

Contents lists available at ScienceDirect

Ocean Engineering

journal homepage: www.elsevier.com/locate/oceaneng

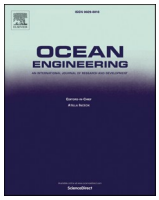

Research paper

Characteristics of ice-structure-soil interaction of an offshore wind turbine

Pengxu Zou [a,b], Jeremy D. Bricker [a,c,*], Ayumi Fujisaki-Manome [d,e], Fernando E. Garcia [a]

[a] Dept. of Civil and Environmental Engineering, University of Michigan, Ann Arbor, MI, 48109, USA
[b] CCCC Guangdong-Hong Kong-Macao Greater Bay Area Innovation Research Institute Ltd., Zhuhai, Guangdong, 519080, China
[c] Dept. of Hydraulic Engineering, Faculty of Civil Engineering & Geosciences, Delft University of Technology, 2600, GA, Delft, the Netherlands
[d] Cooperative Institute for Great Lakes Research, University of Michigan, Ann Arbor, MI, 48108, USA
[e] Climate & Space Sciences and Engineering, University of Michigan, Ann Arbor, MI, 48108, USA

ARTICLE INFO

Keywords:
Ice-structure-soil interaction
Offshore wind turbine
Dynamic response
Ice loads
Glacial soils
Conical structures

ABSTRACT

This research investigates the dynamic response of offshore wind turbine (OWT) systems subject to ice-structure-soil interaction (ISSI). To simulate the behavior of level ice sheets, a coupled approach involving the cohesive element method (CEM) and the finite element method (FEM) is applied. For soil-structure interaction (SSI), the Mohr–Coulomb (M-C) model is employed to accommodate glacial soils. A three-dimensional model for ice-OWT-soil interactions is established using LS-DYNA, focusing on the North American Great Lakes region. The impact of factors, including conical structure geometry, ice loading conditions, and soil characteristics, on the actions of ice and the displacement of the OWT structure, is systematically assessed. The results show a notable reduction in horizontal ice forces when a conical structure is used, underscoring its potential to enhance the stability of an OWT. Additionally, lower ice loading height results in increased ice force and reduced structural displacement. Furthermore, variations in soil properties, specifically elastic shear modulus, cohesion and angle of internal friction, exert a significant influence on OWT dynamics. The elastic shear modulus of glacial soils impacts the displacement of the OWT structure, posing a threat to structural stability. In addition, reduced cohesion and friction angle contribute to greater structural displacement.

1. Introduction

The advancement of offshore wind energy is imperative in addressing the escalating demand for sustainable power sources. Nevertheless, within frigid locales characterized by icy conditions, offshore wind turbines (OWTs) are susceptible to severe damage due to the imposition of ice loads. The Great Lakes region, renowned for its abundant wind resources, stands as a frontier in the development for renewable energy within the United States. For example, the Lake Erie Energy Development Corporation (LEEDCo) is planning to create a demonstration wind farm with a capacity to generate 20.7 MW of electricity in Lake Erie, situated in close proximity to Cleveland, Ohio, in the forthcoming years. Given the persistent presence of lake ice in the shallow waters of Lake Erie during the winter months, the OWT must be designed resilient against the combined loading effects of lake ice and the glacial lakebed which the wind turbine tower is founded. Consequently, there exists a compelling need to gain comprehensive insights into the intricate interactions between ice and OWT foundations, a prerequisite for the development of resilient designs capable of withstanding the distinctive challenges posed by ice-induced loading. Furthermore, given that OWTs are firmly founded to the seabed and embedded within the surrounding soils, the properties of the underlying soil strata exert a substantial influence on the dynamic response exhibited by OWTs. As such, comprehension of ice-structure-soil interaction (ISSI) in the context of OWTs is indispensable, as it serves as the linchpin for ensuring the safety and structural integrity of the entire system.

It is noteworthy that the behavior of the soil-OWT system is inherently nonlinear, with the lateral dynamic ice loads that are counteracted through the intricate interplay between the soil and the OWT. This nonlinearity introduces formidable challenges when predicting the dynamic response of OWTs in icy conditions. Key determinants that exert a significant influence on the ISSI encompass factors such as ice properties, ice loading locations, OWT geometry, and soil characteristics.

Regarding ice properties, comprehensive experimental studies have been conducted to elucidate ice behavior and ascertain the frequency lock-in conditions of cylindrical structures (Hendrikse and Metrikine, 2016), (Hammer et al., 2023), (Nord et al., 2015). For numerical simulations, the coupling of the Cohesive Element Method (CEM) with the

* Corresponding author. Dept. of Civil and Environmental Engineering, University of Michigan, Ann Arbor, MI, 48109, USA
E-mail address: jeremydb@umich.edu (J.D. Bricker).

https://doi.org/10.1016/j.oceaneng.2024.116975
Received 23 November 2023; Received in revised form 22 January 2024; Accepted 30 January 2024
Available online 3 February 2024

Finite Element Method (FEM) has proven to be an efficacious approach for simulating ice-structure interactions (Konuk et al., 2009a), (Lu et al., 2014). This computational approach has facilitated investigations into the influence of ice properties, including ice drift velocity and ice thickness, on structural response, fatigue damage, and energy analysis of OWTs (Liu et al., 2023), (Shi et al., 2023), (Zou et al., 2023a). Furthermore, the impacts of wind speed and ice-wind misalignment angle on the dynamic response of the OWT subject to ice loading have been investigated (Zou et al., 2023a).

Regarding the location of ice loading on the OWT, it is noteworthy that the analysis of ISSI presents distinctive complexities compared to conventional pile foundation design. ISSI causes lateral deformation, leading to displacement in the adjacent soils, and as the magnitude of lateral soil displacement intensifies, it augments the restraint imposed on the OWT. This dynamic interplay between the OWT and the soil constitutes an intricate relationship. While the effects of vertical loads on vertical piles are well-documented, research on vertical piles under lateral loads remains limited (Kavitha et al., 2016). Furthermore, in light of the persistent effects of climate change, it is imperative to design and operate OWTs with flexibility and adaptability to accommodate shifting ice loading patterns. Taking the North American Great Lakes (hereafter referred to as the Great Lakes) as an illustrative example, although they lack substantial astronomical tides akin to ocean shorelines, they experience fluctuations in water levels across various temporal and spatial dimensions. Over the past 10,000 years, Great Lakes water levels have oscillated by tens of meters due to climate change (Mickelson et al., 2004). Ice acting at different elevations of the OWT foundation can engender varying dynamic response, thereby impacting the overall stability and safety of OWTs. Consequently, it is imperative to conduct further investigations to discern how the location of ice loading influences the dynamic response of an OWT.

The geometry of the OWTs plays a pivotal role in the dynamics of ISSI. In regions prone to ice cover, the adoption of a conical-shaped ice-breaking structure is a common practice in OWT design due to its symmetrical plan shape. This conical structure serves as a critical component in the ice-breaking and protection mechanisms for OWTs operating in cold climates. Shi et al. (2023) investigated the dynamic ice loads and responses under varying ice-breaking cone angles, offering insights into the optimal cone angle for specific conditions. Sand and Horrigmoe (1998) employed a nonlinear finite element analysis to account for the effects of cone angle and the friction coefficient between ice and the structure on ice-breaking forces. Additionally, Di et al. (2017) and Long et al. (2020) delved into the analysis of cone diameter and cone angle effects on ice loads and ice-breaking length using the Discrete Element Method (DEM). Nevertheless, a comprehensive comparison between scenarios with and without the presence of a conical structure is warranted, and should account for in the complexities of the underlying ISSI phenomena.

Regarding soil properties, the interplay between the foundation of an OWT and the underlying soil has a profound influence on the structural behavior, stability, and performance. The dynamic response of the OWT, encompassing parameters such as its natural frequency, internal forcing, and damping characteristics, can be significantly modulated by the interaction between the foundation and the soil (Rodriguez-Galván et al., 2023) and (Yang et al., 2019). Zhu et al. (2021) conducted analyses that revealed a reduction of approximately 9.7 % in the natural frequencies of the tower when considering soil-structure interaction (SSI) effects in comparison to scenarios without SSI (fixed bottom boundary scenario). Araz (2022) conducted time-domain analysis for seismic-induced vibrations of a multi-story building, and found that SSI plays a crucial role in shaping the optimal design and efficacy of the tuned mass damper inerter (TMDI). Furthermore, the wind response of wind turbines experiences an amplification effect when SSI is taken into account (Gaur et al., 2020). In addition, the impact of soil type on structure dynamic response is intricate. Soil type exerts a substantial influence on the control performance of tuned tandem mass dampers, particularly in mitigating vibrations induced by seismic events (Araz and Farsangi, 2023). Conversely, the effects of SSI can be disregarded in scenarios where structures are erected on stiff soil conditions (Araz et al., 2023). Despite these significant findings, investigations into the role of SSI in ice-OWT collision simulations have been limited due to the intricate nature of ISSI. Shi et al. (2023) established a coupled ice-OWT-soil interaction model and employed the apparent fixity method to simulate SSI effects, simplifying them in terms of horizontal forces and bending moments while investigating foundations in only sandy soil. Zhu et al. (2021) harnessed self-excited vibration theory (SVT) to simulate ISSI and delineated ice-induced frequency lock-in in OWTs, with soil effects being represented through translational and rotational spring elements. Similarly, Liu et al. (2023) and Wang et al. (2022a) formulated a coupled ice-OWT-soil interaction model, incorporating non-linear *p-y* spring elements to address SSI effects.

It is worth noting that the non-linear behavior of SSI is frequently modeled using simplified static forces or equivalent *p-y* soil springs in conjunction with finite element programs (Gholipour et al., 2018). However, the *p-y* curve model tends to overestimate pile-soil stiffness, particularly for large-diameter single piles (ling Zhang et al., 2023), and its accuracy diminishes when the length-diameter ratio of the pile exceeds 7 (Wang et al., 2022b). Therefore, the accuracy of the *p-y* curve model in ISSI simulations for the OWTs is questionable. The imperative lies in the utilization of a more reliable methodology for predicting OWT behavior when embedded in soils, particularly when dealing with glacial soils as observed in the Great Lakes. The geotechnical characteristics of glacial soils, including factors such as particle size distribution, density, permeability, stiffness, dilatancy, and strength, exhibit considerable variability (Clarke, 2017). These variations in soil properties can exert a substantial influence on the OWT's capacity to withstand ice forces and maintain stability. Hence, it becomes indispensable to embark on further investigations to elucidate the geotechnical properties of glacial soils and their ramifications on OWT behavior and performance.

To address the aforementioned research gap, a three-dimensional ice-OWT-soil interaction model implemented using LS-DYNA within the context of the Great Lakes region is established, with the objective of acquiring essential insights into ice forces, OWT displacements, and stress distributions within the OWT foundation. FEM is employed to tackle complex geotechnical issues owing to its robust capabilities in nonlinear and multi-physics interaction analysis (Mokhtar et al., 2014). A soil continuum model is adopted, encompassing a comprehensive representation of soil behavior to account for varying glacial soil properties for ISSI simulations. Furthermore, coupled CEM-FEM is utilized to simulate dynamic ice loads. The impact of critical parameters on the mechanical dynamic response of an OWT is investigated, including the presence of conical structures, the ice loading location on the OWT, and the underlying soil properties.

The structure of this paper is organized as follows: Section 2 introduces the case study and outlines the modeling setup, with a description of the properties and materials employed for characterizing ice, the OWT, and the soil; Section 3 encompasses the verification of the numerical model, where simulated ice forces and structural deflections are compared with theoretical and experimental data; In Section 4, a sensitivity analysis is conducted, exploring the influence of key factors including the presence of conical structures, ice loading locations, and soil properties on the dynamic response of an OWT.

2. Model description

In this section, a comprehensive three-dimensional ISSI model is formulated to simulate the dynamic response of a wind turbine on a monopile foundation, which is subject to ice loading and founded in glacial soil in Lake Erie. A detailed exposition of the properties and materials of the ice, OWT, and soil in the numerical model is provided.

2.1. Modeling of level ice sheet

In this study, a coupled CEM-FEM for modeling ice material behavior is adopted. This combines bulk elements to capture localized ice crushing, plasticity, and viscous effects with cohesive elements to simulate the formation of multiple branching cracks and the fracture behavior of the ice material. To characterize the ice material's response, an elasto-plastic constitutive law for the bulk ice elements is utilized, representing isotropic behavior. The cohesive forces within the cohesive elements are determined by the material's traction-separation law. The ice mass is represented using bulk finite elements incorporating a nonlinear plastic-kinematic material model (Wang et al., 2022a), (Wang et al., 2020), (Gürtner et al., 2008), (Xing et al., 2023). The constitutive behavior of bulk ice elements is investigated through a stress-strain relationship, employing an elasto-plastic constitutive law to characterize ice behavior. Fig. 1(a) illustrates the elastic behavior of ice, characterized by an elastic modulus E, until the yield stress Y_0 is attained. Upon reaching this point, a linear softening process ensues, and a crushing-induced crack progressively develops following a hardening law until it reaches the plastic strain ε_c. Ultimately, the ice undergoes complete crushing failure, transitioning into a viscous fluid state until it reaches the failure strain ε_f. Elements with plastic strain exceeding 0.7 and exhibiting significant distortion are subsequently removed (Xing et al., 2023). The stress-separation relationship of CEM is depicted in Fig. 1 (b). The cohesive element material initially behaves elastically until a critical crack separation distance δ_0 is reached, corresponding to the maximum allowable traction T_0. Beyond this point, damage occurs, and the material follows. At this stage, the cohesive element is damaged beyond this point, following a linear softening curve until the separation δ_1 is attained. The cohesive element is subsequently removed, resulting in the explicit formation of a crack. The total energy dissipation is equal to the cumulative area (i.e., regions I and II). It is noteworthy that the energy associated with Region II can be recovered during the crack unloading process (Konuk et al., 2009b).

The ice sheet is 36 m in length, 28 m in width, and 0.4 m in height. The ice drift speed is 0.4 m/s, moving toward the OWT structure. The bulk ice mass is discretized using finite elements, while cohesive elements are strategically positioned along the internal horizontal and vertical boundaries of these bulk elements. To model the level ice sheet, 8-node hexahedron elements are employed, with 4-point cohesive elements placed on the internal surfaces of each hexahedron element. Both the vertical and horizontal cohesive elements share the same cohesive properties, ensuring consistent behavior across the ice sheet. Fig. 2(a) provides a visual representation of the coupled bulk elements and cohesive elements within the level ice sheet model. It's worth noting that the ice breaking length is influenced by several factors, including ice thickness, ice drift speed, ice strength, and the diameter of the structure. The selection of mesh sizes for both bulk and cohesive elements should be consistent with the observed ice breaking lengths from practical field test data (Lu et al., 2014), (Wang et al., 2020). Given the substantial surface area of the Great Lakes and the influence of wind wave actions, the ice cover in this region exhibits characteristics similar to coastal sea ice (Shen et al., 2004). In accordance with ice-image data collected from a field monitoring system in the Bohai Sea (Wang et al., 2022c), a mesh size of 0.8 m is used, and the range of mechanical properties for sea ice (e.g., Young's modulus) based on (Hilding et al., 2011; Leppäranta, 2011; Moreau et al., 2020; Skatulla, 2022; Xing et al., 2023) is utilized, to represent the similarities to sea ice yet acknowledge the impact of absence of brine pockets. Notably, field tests conducted by (Gürtner et al., 2010) unveiled a sea ice fracture energy range of 23–47 J/m^2. However, when considering numerical models employing CEM to simulate ice failure, the choice of a higher fracture energy is often favored due to variations in loading rates in simulations and laboratory tests, as well as disparities in ice element sizes (Lu et al., 2014). According to (Liu et al., 2023), a fracture energy of 100 J/m^2 is applied. A free boundary is defined on the ice edge in contact with the conical structure, while fixed boundaries are imposed on the three other edges of the ice sheet. An elastic water column beneath the ice is incorporated for ice sheet support. Furthermore, the *CONTACT_AUTOMATIC_NODES_TO_SURFACE* algorithm in LS-DYNA is defined between the ice and the water column, to avoid ice penetrations at the interface. The "*CONTACT_AUTOMATIC_NODES_TO_SURFACE*" algorithm is a one-way contact type allowing for compression loads to be transferred between the water column and ice cover. However, the penetration of nodes on the ice cover through the water column is not considered in adaptive remeshing. According to the mechanical properties of sea ice used in (Lu et al., 2014), (Xing et al., 2023), (Hilding et al., 2011), an overview of material properties utilized for the bulk ice and cohesive elements in the numerical model is shown in Table 1.

2.2. Modeling of offshore wind turbine

The monopile foundation is chosen for analysis because it is the most common foundtion type for OWT's worldwide, and, due to its relatively low cost, is expected to be increasingly utilized in the US. The example OWT has a capacity of 3.45 MW, and it comprises major components such as the foundation, tower, nacelle, and rotor with blades (Wagner et al., 2018). In the numerical model, the OWT structure, including the tower and foundation, is represented using eight-node brick elements with an elastic material behavior that accommodates bending in flexure. Mass elements are placed at the top of the tower to account for the weight of the nacelle and hub. Vertical translation of bottom boundary of the OWT is constrained. To simulate scenarios involving ice-OWT collisions in LS-DYNA, a contact algorithm *ERODING_NODES_TO_SURFACE* between the ice and the OWT is employed. Within the "*ERODING_NODES_TO_SURFACE*" contact algorithm, the slave side

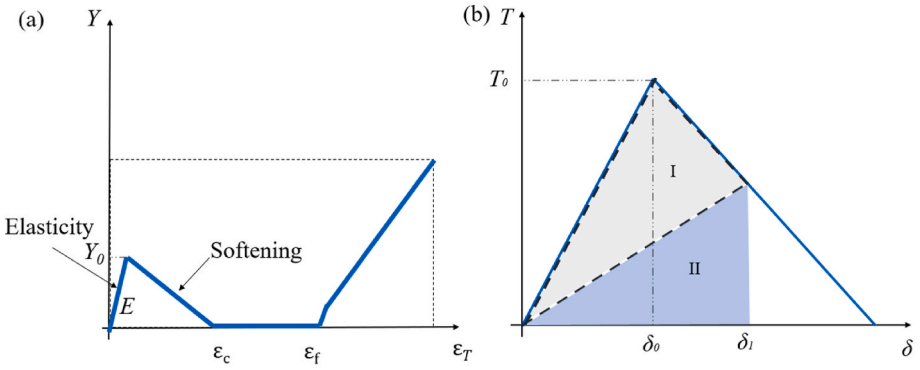

Fig. 1. Constitutive laws for (a) solid ice elements; (b) cohesive elements; where E is elastic modulus of the material; Y is stress; Y_0 is yield stress; ε_c is strain after the softening process; ε_f is failure strain; ε_T is true strain of bulk elements; δ is the separation distance; δ_0 is critical crack separation distance; δ_1 is failure separation distance; T represents traction; T_0 denotes the critical traction; Regions I and II represent the energy dissipation area.

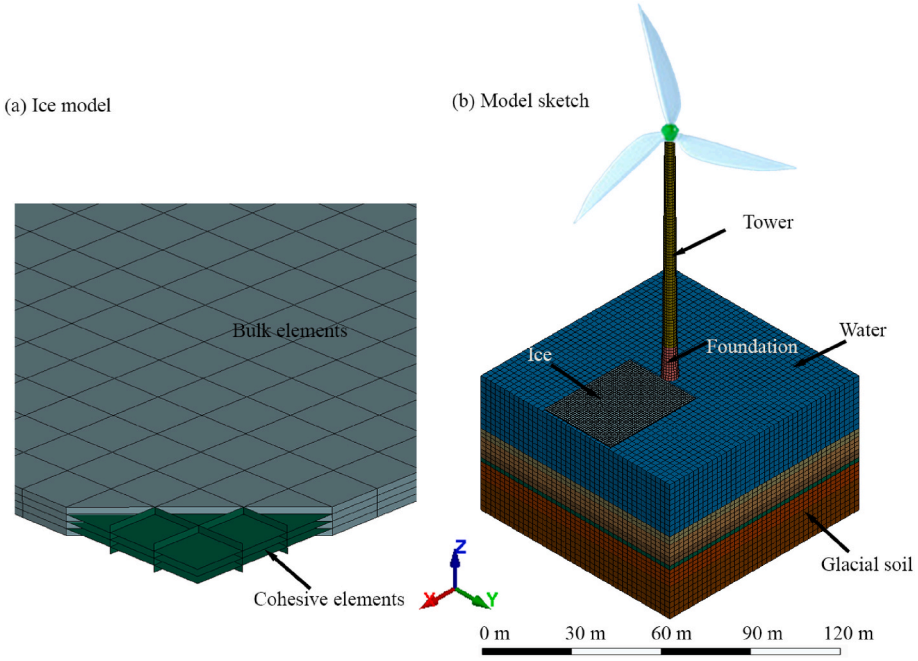

Fig. 2. Numerical model sketch (a) bulk and cohesive elements in the ice model; (b) ice-OWT-soil interaction model (colors below the water column represent various soil layers).

Table 1
Ice material properties.

	Bulk ice element	Cohesive element
Young's modulus	5 GPa	5 GPa
Yield stress	1.8 MPa	1.1 MPa
Density	900 kg/m3	900 kg/m3
Fracture energy	–	100 J/m^2

encompasses the comprehensive set of nodes on the ice cover, while the master side corresponds to the contact surface of the OWT foundation. The updating of the contact surface occurs as elements on the free surface are deleted in accordance with material failure criteria.

This algorithm takes into account sliding and frictional forces during ice contact, with dynamic and static frictional coefficients of 0.3 to represent the frictional behavior between the ice and the OWT components during the collision.

The dimensions of the OWT components are as follows: The hub height is 90.67 m. The base and top diameters of the tower are 3.07 m and 4.5 m, respectively. The water depth at the project site in Lake Erie is approximately 19 m. The total height of the monopile foundation is 61 m, which includes 12 m above the waterline, 19 m submerged in water, and 30 m within the glacial soil. The cross-sectional diameter of the foundation varies from 4.5 m to 6.0 m. Specifically, the diameters at the waterline and within the glacial soils are 5.5 m and 6.0 m, respectively. The masses of rotor-nacelle assembly (RNA) and tower are 188.23 t and 347.5 t, respectively (Wagner et al., 2018), (Beik and Al-Adsani, 2020). The materials used for the OWT components, including the wind turbine tower and monopile foundation, are constructed from S355 structural steel. The material properties are as follows: Young's modulus of 210 GPa; Poisson's ratio of 0.3; density of 7850 kg/m^3. To simplify the model, the model tower is simulated using an equivalent density that ensures it has the same mass and stiffness as the actual tower accounting for its actual thickness. The equivalent model tower density and Young's modulus are 394 kg/m^3 and 7.88 GPa, respectively.

2.3. Modeling of soil

A geotechnical survey conducted by Hull & Associates, Inc. (2016) (Wagner et al., 2018) was instrumental in characterizing the glacial drift soil composition for the proposed electrical substation of the project in Lake Erie. This glacial drift consists of varying proportions of gravel, sand, silt, and clay, and its key physical properties, derived from geotechnical field tests, are presented in Table 2. It is noted that the shear modulus of the soil is not available in the geotechnical survey data. Based on the shear stiffness profiles derived from in-situ and laboratory tests conducted at the Cowden till site, it is observed that the shear moduli of the glacial tills typically fall within the range of 20–170 MPa (Ushev, 2018). Given the prevailing elastic behavior of the soil at small strain levels, a shear modulus of 150 MPa for all soil layers has been chosen in the model. In this research, the volume expansion of soil is not considered, the dilation angle is assumed to be zero, indicating there is no volume change during shearing.

The glacial soil is modeled by eight-node brick elements, and the soil material is represented using an elastic-perfectly plastic constitutive Mohr-Coulomb model, which is suitable for glacial soils (Jayasinghe et al., 2020). The Mohr-Coulomb criterion is expressed as follows:

$$\tau = c + \sigma \tan(\varphi) \quad (1)$$

Where τ is the maximum shear stress on a plane; σ is the normal stress on that plane; c is cohesion; φ is the angle of internal friction.

The impact of the soil boundary on the pile-soil interaction becomes negligible when the distance between the pile and the soil boundary exceeds six times the diameter of the pile (Yuan et al., 2022). Therefore, to mitigate boundary effects, the distance between the pile and the soil boundary in the model is 40 m. 8-node hexahedron elements with a mesh size of 1.5 m have been selected for glacial soil modeling. For modeling the interface between the OWT and soil, the Coulomb friction formula is applied, employing a tangential friction coefficient of 0.36 (the interface friction angle is approximately two-thirds of the soil's internal friction angle, as suggested by (Sheng et al., 2007)). Regarding boundary conditions in the model: the bottom of the mesh represents bedrock, and it is assumed to be fixed in all directions; The four side boundaries are treated as symmetry planes, constraining translatory

Table 2
Generalized soil profile.

Material	Depth (m)	Buoyant unit weight (kg/m^3)	Elastic shear modulus (MPa)	Cohesion (kPa)	Friction angle (deg.)	Poisson's Ratio
Fill-medium dense silty sand	0–3.05	842	150	–	28	0.30
Fill-loose sand	3.05–7.62	842	150	–	23	0.25
Medium dense to dense silty sand	7.62–10.67	922	150	–	30	0.30
Loose to medium dense silty sand with gravel	10.67–12.19	962	150	–	23	0.25
Soft to medium stiff lean clay	12.19–18.29	1002	150	35.91	–	0.40
Medium stiff to stiff lean clay	18.29–30	1002	150	47.88	–	0.45

displacements normal to the plane; Non-reflecting boundaries are imposed on the sides to prevent artificial stress wave reflections and mitigate their impact on soil vibration responses; To account for geostatic stresses in the soil, self-weight loads are introduced using the dynamic relaxation option in LS-DYNA. The illustration of the ice-OWT-soil interaction model is depicted in Fig. 2(b), with a representation of the blades and hub included for visual aesthetics. Water is modeled as an elastic foundation and the buoyancy force acting on the ice sheet can be balanced by its self-weight. The hydrostatic pressure is considered as an external load, acted on the OWT foundation below waterline, as depicted in Fig. 3(a). It should be noted that the approach taken for the soil analysis is strictly pseudo-static and excess pore pressures are not generated. Fig. 3(b) presents the results from the initial state prior to the dynamic analysis of the ice-OWT-soil interaction. The influence of the gravitational field on glacial soil is considered, leading to a generally uniform vertical effective stress at the same depth. The effective stress, pore water pressure and total stress of glacial soils at the initial state is shown in Fig. 3(c). The reliability of the distribution of the initial stress level in the glacial soils establishes a solid foundation for subsequent dynamic analyses. Given the primary objective of this study on analyzing the dynamic response of the OWT once the foundation is in place, the transient and complex interactions associated with the installation and construction processes are not considered.

2.4. Model tests

Various numerical model tests are conducted to investigate the impact of different factors on the ISSI and the vibration characteristics of an OWT. The test conditions of the numerical models are described in this section.

To evaluate the effects of a conical structure on ISSI, the dynamic response of an OWT with and without a conical structure is compared. The conical structure in this study has a cone angle of 45°, a total height of 5.5 m, and a height above the waterline of 1.5 m. The conical structure in this study is used to break the oncoming ice sheet by deflecting it upwards (the level ice approaches the upper part of the cone).

To evaluate the effects of ice loading location on ISSI, ice loading points on the OWT are imposed at different depths, specifically at $z = 0$ m, −5 m, and −10 m, relative to a reference lake water depth of 19 m. These depths correspond to different water levels and represent varying ice loading scenarios.

To evaluate the effects of soil properties on ISSI, a sensitivity analysis to soil shear modulus, cohesion and friction angle is conduced. The variations in soil properties are as follows: Shear modulus values of all soil layers in the base model (Table 2) are multiplied by factors of 0.5, 1.0, and 1.5 (0.5G, 1.0G, and 1.5G) to investigate the influence of shear modulus of soil on ISSI. Based on the category indicated in (Araz et al., 2023), the 0.5G, 1.0G, and 1.5G cases correspond to soft soil, stiff soil, and very stiff soil types, respectively. It should be noted that shear modulus degradation is not considered in this study; Cohesion values of the clay soil layers (bottom two layers) in the base model (Table 2) are multiplied by factors of 0.5, 1.0, and 1.5 (0.5c, 1.0c, and 1.5c) to investigate the influence of cohesion on ISSI. For the friction angles of the glacial soils, Chung & Finno (Chung and Finno, 1992) investigated the mechanical properties of Chicago glacial clay using standard 24-h load-increment consolidation tests and triaxial tests, showing that the average angle of friction values of 28.3 and 34.6° for compression and extension loadings, respectively. Considering the relatively low friction angles in the glacial soil of Lake Erie (Table 2), the strength induced by friction angle of the top four layers of soils in the base model is multiplied by factors of 80 %, 100 %, and 120 % (i.e., 0.8tanφ, 1.0tanφ, and 1.2tanφ) of its original value. The friction angle values range from 18–34°. The test conditions for the sensitivity analysis are outlined in Table 3.

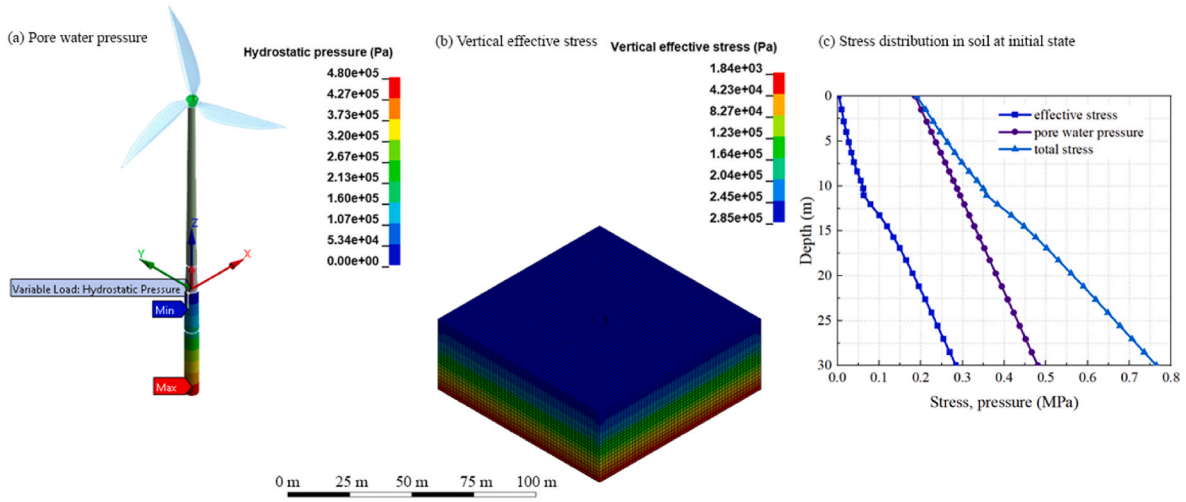

Fig. 3. Initial state results. (a) hydrostatic pressure on the OWT; (b) vertical effective stress of glacial soils; (c) effective stress and pore pressure distributions along z direction in the soil.

Table 3
Test conditions.

Case	Conical Structure	Ice loading location	Shear modulus	Cohesion	Friction angle
Base	Without cone	$z = 0$	G	c	$\tan\varphi$
Case1	With cone	$z = 0$	G	c	$\tan\varphi$
Case2	Without cone	$z = -5$	G	c	$\tan\varphi$
Case3	Without cone	$z = -10$	G	c	$\tan\varphi$
Case4	Without cone	$z = 0$	$0.5G$	c	$\tan\varphi$
Case5	Without cone	$z = 0$	$1.5G$	c	$\tan\varphi$
Case6	Without cone	$z = 0$	G	$0.5c$	$\tan\varphi$
Case7	Without cone	$z = 0$	G	$1.5c$	$\tan\varphi$
Case8	Without cone	$z = 0$	G	c	$0.8\tan\varphi$
Case9	Without cone	$z = 0$	G	c	$1.2\tan\varphi$

3. Model validation

The validation of the model is crucial to ensure the accuracy and reliability of the numerical setup. However, due to the inherent challenges of recreating combined ice-soil-foundation loading in laboratory settings, access to experimental data for verification is limited. Additionally, numerical models that accurately capture ice-OWT interaction effects are lacking. Therefore, in this section, separate validations for ice-OWT interaction and soil-structure interaction are performed.

3.1. Mesh size sensitivity analysis

To assess mesh convergence and validate computational results, a sensitivity analysis on element sizes of soil and structure are performed by systematically varying the maximum element size and comparing the time histories of ice force. Table 4 presents the results of the mesh sensitivity analysis, with the "Base" case as a reference (Table 3). The analysis reveals that the peak ice force is approximately 15 % underestimated when using a mesh size of 3 m. Furthermore, Fig. 4 illustrates the time histories of ice force, indicating more fluctuating patterns during the unloading stage for this larger mesh size.

However, with maximum element sizes of 1.0 m and 1.5 m, a consistent peak ice force is observed, demonstrating both mesh convergence and numerical stability. To optimize computational efficiency, a maximum mesh size of 1.5 m is selected for all analyzed cases. This choice ensures reliable results while mitigating computational costs.

3.2. Ice force validation

To validate the dynamic ice load on the OWT, the numerical simulation results of the base model is compared with engineering design specifications outlined in ISO 19906 (ISO, 19906, 2019). When ice crushing occurs against a structure, the global ice action normal to the surface can be calculated by:

$$F = p_G A \tag{2}$$

Table 4
Mesh sensitivity analysis.

Maximum mesh size (m)	Total element number	Averaged ice peak force (MN)
3	40,317	4.67
1.5	193,146	5.32
1	249,336	5.25

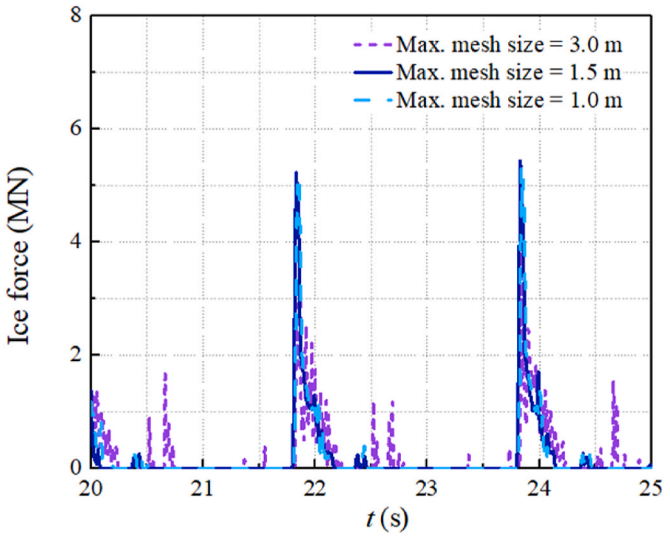

Fig. 4. Mesh sensitivity results.

where F is the ice force; p_G is the ice pressure averaged over the nominal contact area; A is the nominal contact area, for an ice cover sheet, A is the product of ice thickness h, and the projected width of the structure w (in meters).

According to ISO 19906 (ISO, 19906, 2019) based on measured data, the global ice pressure can be determined by:

$$p_G = C_R \left(\frac{h}{h_1}\right)^n \left(\frac{w}{h}\right)^m \tag{3}$$

where h_1 is a reference thickness of 1 m; m is an empirical coefficient equal to -0.16; n is an empirical coefficient, equal to $-0.50 + h/5$ for $h < 1.0$ m, and -0.30 for $h \geq 1.0$ m; C_R is the ice strength coefficient (MPa).

The value of C_R for the Great Lakes is not provided in (ISO, 19906, 2019), but it can be assumed as 2.8 MPa and 1.8 MPa based on first-year and multi-year data from Beaufort Sea and the conditions in the Baltic Sea, respectively (ISO, 19906, 2019). Fig. 5(a) displays a comparison of ice force values obtained from the numerical model and empirical results based on Eqs. (2) and (3). The numerical model's maximum and mean ice forces in the x direction are 5.2 MN and 0.25 MN, respectively. This comparison shows that the maximum ice force from the numerical results is within the range of calculated results. This demonstrates the accuracy of the ice force and ice-OWT interaction within the numerical model. However, it's worth noting that current design specifications for ice load only consider the extreme static ice force, not accounting for ice-induced vibrations or the detailed ice-structure interaction process. Hence, it is imperative to utilize the high-fidelity numerical approach for conducting the ISSI simulations.

3.3. Soil-structure interaction model validation

To validate the soil-structure interaction model, field test data from a lateral loaded pile are employed (Ismael, 1998). The pile has a diameter of 0.3 m and a length of 5 m, while the soil is medium dense silty sands with properties listed in Table 5. The soil properties utilized in the analysis are derived from the selected site in Kuwait (Ismael, 1998), characterized by the presence of added cementation extending from the ground surface downwards. The cementation within the soil introduces both a cohesion intercept and an augmentation in the angle of shearing resistance. 8-node hexahedron elements are employed to model both the pile and the surrounding soil. The overall dimensions of the soil domain are 3.6 m in length and 3.6 m in width. The soil is divided into surface and bottom layers, with depths of 3.5 m and 2.5 m, respectively.

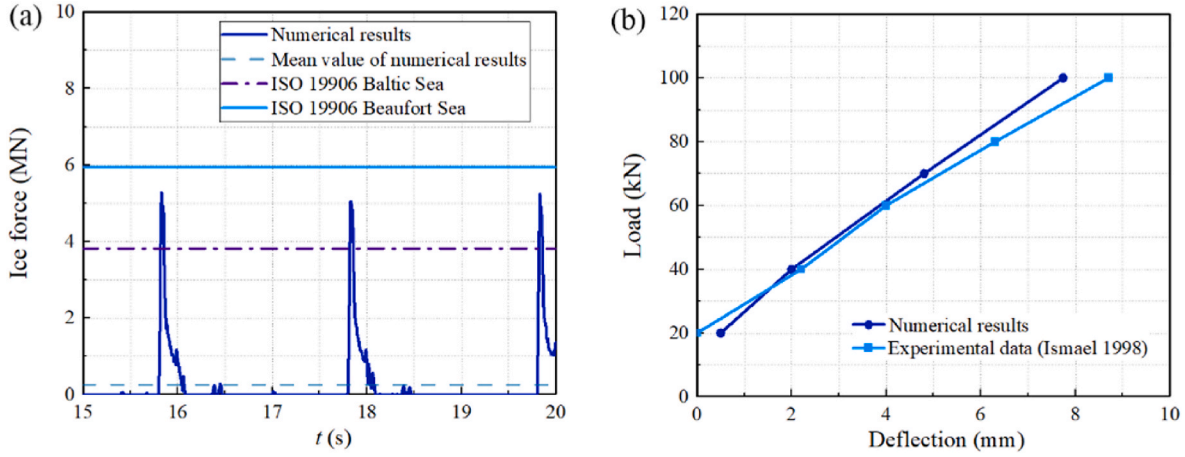

Fig. 5. Numerical results validation (a) ice force; (b) deflection curve of pile top under various load.

Table 5
Material properties of the soil layers and pile.

Material	Weight (kN/m^3)	Young's modulus (Pa)	Cohesion (kPa)	Friction angle (deg.)	Poisson's Ratio
Medium dense silty sand	18	1.3×10^7	20	35	0.30
Medium dense to very dense silty sand	19	1.3×10^7	–	45	0.30
Pile	25	2.2×10^{10}	–	–	0.15

Symmetric side boundary conditions of the soil are applied. The *CONTACT_AUTOMATIC_NODES_TO_SURFACE* algorithm is defined between the soil and the pile with an angle of wall friction of 10 deg. ($\sim 0.3\varphi$), to simulate the SSI scenario. A horizontal external force with varying magnitude is applied in the x direction on the top of the pile. A static analysis of the SSI process is considered. An explicit solver with explicit time integration in LS-DYNA is adopted. The numerical model configuration and the numerical results are shown in Fig. 6. The pile is extracted from the mesh to present the deflection, as depicted in Fig. 6 (c).

Fig. 5(b) illustrates a comparison of the lateral load deflection response between the experimental data and numerical simulations. The deflections at the pile top under an external load of 100 kN are 8.6 mm and 7.7 mm for the experimental data and numerical results, respectively, with a relative error within 10 %. This comparison demonstrates that the numerical method effectively incorporates nonlinear soil-structure interaction effects under quasi-static soil conditions, thus validating the soil-structure interaction model. It is pertinent to acknowledge that the validation of the model for a monotonic loading problem does not inherently extend its validity to harmonic dynamic loading. However, in the context of quasi-static soil conditions, this distinction proves inconsequential.

4. Results

This section delves into a comprehensive analysis of the numerical results obtained from the ISSI model under various conditions, including scenarios with and without a conical structure, different ice loading locations, and varying soil properties.

4.1. Modal analysis

To gain insights into the dynamic behavior of the OWT, a modal analysis is conducted to calculate the fundamental eigenfrequencies of the structure, which helps to understand the natural vibrational modes of the OWT and provides critical information about its dynamic response characteristics (Zou et al., 2022), (Zou et al., 2023b). To better understand the effects of SSI on the natural frequencies of the OWT, a comparative study is conducted with and without consideration of SSI (the OWT is fixed at the base). The results are depicted in Table 6, showcasing the natural frequencies and mode shapes of the OWT. It shows that, when SSI is taken into account, both the tower bending and

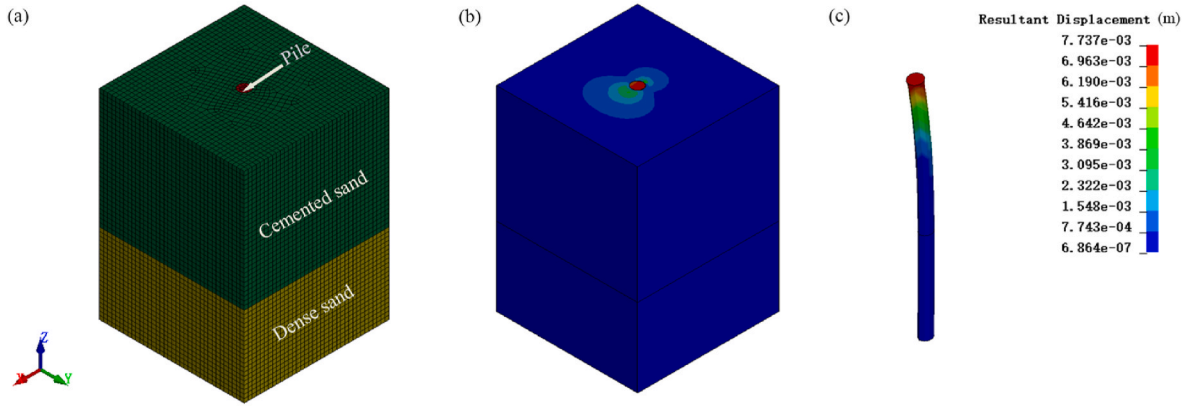

Fig. 6. Soil-structure interaction model (a) mesh configuration; (b) resultant displacement distribution with the external force of 100 kN in the x direction; (c) deflection of the pile in the soil.

Table 6
Natural frequencies of the OWT.

Mode number	Natural frequency (Hz)		Mode shape
	Consider SSI	Neglect SSI	
1	0.252	0.255	Fore-aft bending mode of the tower
2	0.252	0.255	Side-side bending mode of the tower
3	1.332	1.824	Fore-aft global bending mode
4	1.334	1.824	Side-side global bending mode

global bending frequencies exhibit decreases of 1.2 % and 37 %, respectively. This can be attributed to the inherent flexibility introduced by SSI to the foundation, leading to a reduction in natural frequencies when compared with the fixed boundary case where SSI is neglected.

4.2. Effects of OWT geometry

To better understand ice actions due to sheet ice and elucidate the influence of the conical structure on ice breaking and structural dynamics, the horizontal and vertical ice forces along with the x displacements at the tower and foundation of the OWT with and without the conical structure (Base case and Case1) are compared.

Fig. 7(a) presents the horizontal ice force for both "with cone" and "without cone" cases. The peak ice force in the "with cone" case, characterized by a sloping structure, is significantly reduced—approximately half that of the "without cone" case, which features a vertical-sided structure. The maximum horizontal ice forces are approximately 3 MN and 5 MN for "with cone" and "without cone" cases, respectively. Due to the broader ice-breaking structure diameter and ice rubble pile-up against the sloping side of the cone, the "with cone" case exhibits a more extended ice-structure contact area and a longer duration of ice-structure interaction. The ice action period can be expressed by L/v (L is the breaking length which is related to the mesh size of the ice and v is ice drift speed). Therefore, for an ice drift speed of 0.4 m/s and ice element size of 0.8 m, the ice action period is 2 s. Notably, the ice action period exceeds the loading and unloading cycle durations in both cases, surpassing the natural period of the OWT. The frequency spectrum analysis reveals intriguing insights into the behavior of the OWT subjected to ice interactions. Fast Fourier Transform (FFT) analysis is performed to illustrate the frequency spectrum of horizontal ice forces, shown in Fig. 7(b). Both cases exhibit peak frequencies corresponding to the ice-breaking frequency and its harmonics (e.g., 0.5 Hz, 1.0 Hz, 1.5 Hz). The "without cone" case displays significantly larger amplitudes at 1–2.5 Hz, while amplitudes beyond 3 Hz are smaller. However, the "with cone" case exhibits an opposite trend. This suggests that the "with cone" case introduces higher-frequency components into the ice force.

Fig. 7(c) portrays the vertical ice force. In the "with cone" case, vertical ice forces are approximately 15 times greater than those in the "without cone" case. The maximum vertical ice forces are approximately 3 MN and 0.2 MN for "with cone" and "without cone" cases, respectively. Notably, the inclined angle of the conical structure (45°) contributes to comparable magnitudes of horizontal and vertical forces in the "with cone" case. Conversely, the "without cone" case experiences horizontal ice forces around 25 times larger than the vertical forces. These observations indicate that the conical structure not only reduces the peak horizontal ice force but also generates a substantial upward

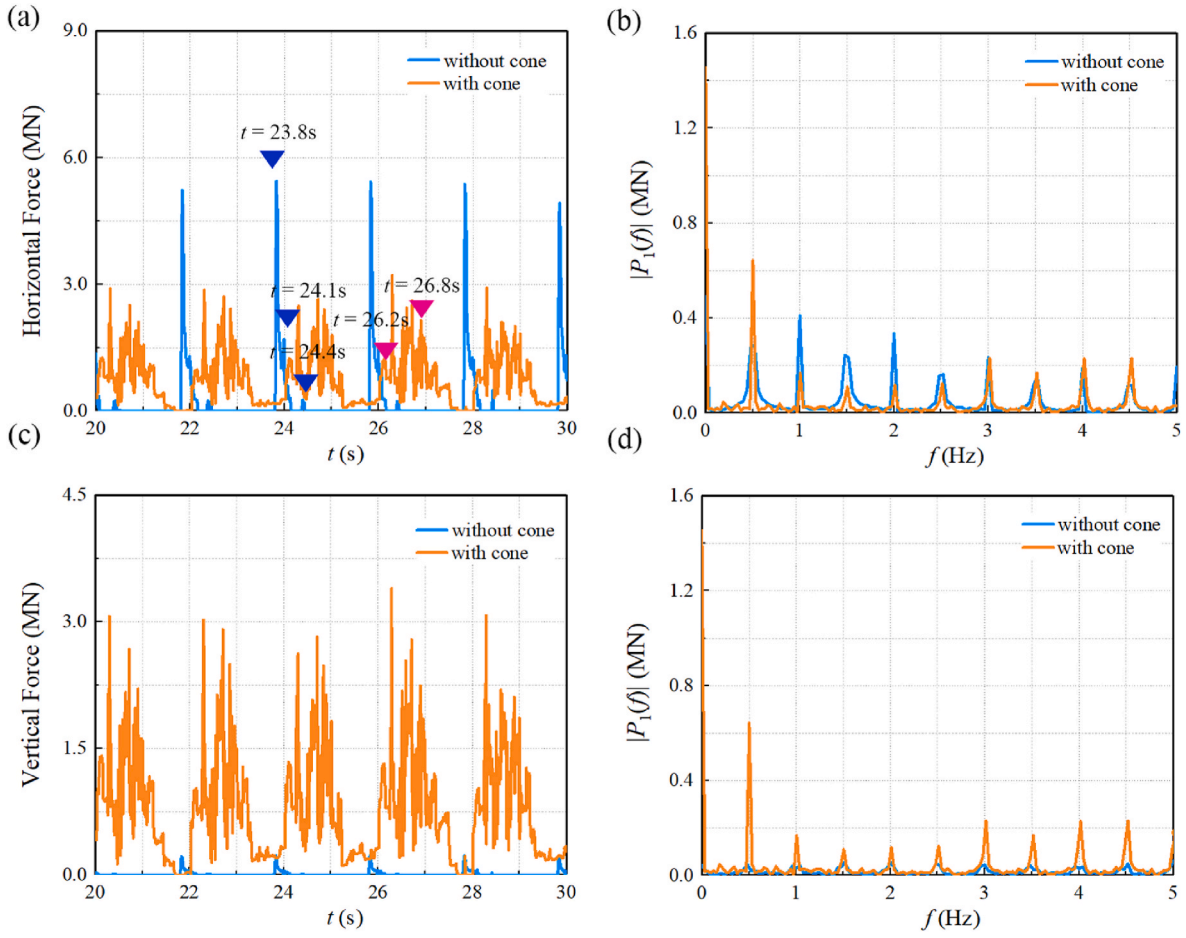

Fig. 7. Time histories and frequency spectra of ice force for the "with cone" and "without cone" cases. (a) time series of horizontal ice force; (b) frequency spectrum of horizontal ice force; (c) time series of vertical ice force; (d) frequency spectrum of vertical ice force.

deflection of the ice sheet, resulting in a downward vertical force. This increased vertical force increases the normal stresses at the point of contact, which enhances the frictional resistance between the OWT and soils. This contributes to the overall safety and stability of the OWT. In contrast, the "without cone" case features a predominantly horizontal ice force, emphasizing the importance of the conical structure's effects on ice interactions. As observed in the horizontal force spectrum, the vertical ice force spectrum shown in Fig. 7(d) also exhibits peak frequencies representing the ice-breaking frequency and its harmonics, with the "with cone" case displaying higher-frequency components ($f >$ 3 Hz).

Notable differences between the cases with and without the cone structure can be observed in the OWT's displacement at the top of the OWT foundation (31 m above the mudline) and the tower (109.67 m above the mudline). At the top of the foundation (Fig. 8(a)), the "with cone" case displays smaller displacements than the "without cone" case. The maximum amplitudes of displacement at the top of the foundation are around 0.009 m and 0.013 m for "with cone" and "without cone" cases, respectively.

Frequency spectrum analysis of foundation displacements (Fig. 8(b)) reveals that the maximum frequency amplitude for "with cone" and "without cone" cases occurs around 0.5 Hz and 1.5 Hz (or 1.0 Hz), respectively. This indicates a longer duration of the ice-OWT interaction process in the "with cone" case compared to the "without cone" case. Notably, a peak frequency at around 1.2 Hz is observed for the "with cone" scenario, corresponding to the structural natural frequency of global bending mode. A secondary peak at approximately 1.3 Hz is evident for the "without cone" case, representing for the natural frequency of the OWT (Table 6). This peak superimposes with the primary peak frequency at 1.5 Hz, resulting in a wider frequency range and a more evenly distributed spectral shape.

At the tower top (Fig. 8(c)), the "with cone" case still results in smaller displacements compared to the "without cone" case. However, the reduction in displacement due to the presence of the cone structure is less pronounced at the tower top. This suggests that the cone's effects are more localized at the elevation where ice collides with the OWT. The maximum amplitudes of displacement at the tower top are 0.014 m and 0.018 m for "with cone" and "without cone" cases, respectively.

For the tower displacement spectrum (Fig. 8(d)), the bending mode of the tower at around $f = 0.25$ Hz with similar spectral amplitudes are activated for both cases. However, the peak frequency in the "with cone" case is slightly lower than in the "without cone" case (as indicated in the red circle). This discrepancy can be attributed to the added weight of the conical structure, which lowers the natural frequency. Moreover, it can be observed that the higher-frequency components ($f > 1$ Hz) play a significant role in the displacement of the "without cone" case. Additionally, due to the superimposed tower natural period vibrations, the time history of the displacement (Fig. 8(c)) exhibits a more irregular pattern compared to that at the foundation top.

To further elucidate the dynamic response characteristics of the OWT influenced by the conical structure, the stress distribution on the OWT foundation, the ice forces, and structural deflections at various time intervals are examined.

The ice action period from 23.7 s to 24.4 s is taken as an illustrative example for the "without cone" case. At $t = 23.7$ s, the ice sheet detaches from the OWT, resulting in minimal ice force and negligible effective stress (Fig. 9). Advancing to $t = 23.8$ s, the ice sheet initiates contact with the OWT, leading to the foundation's effective stress reaching its

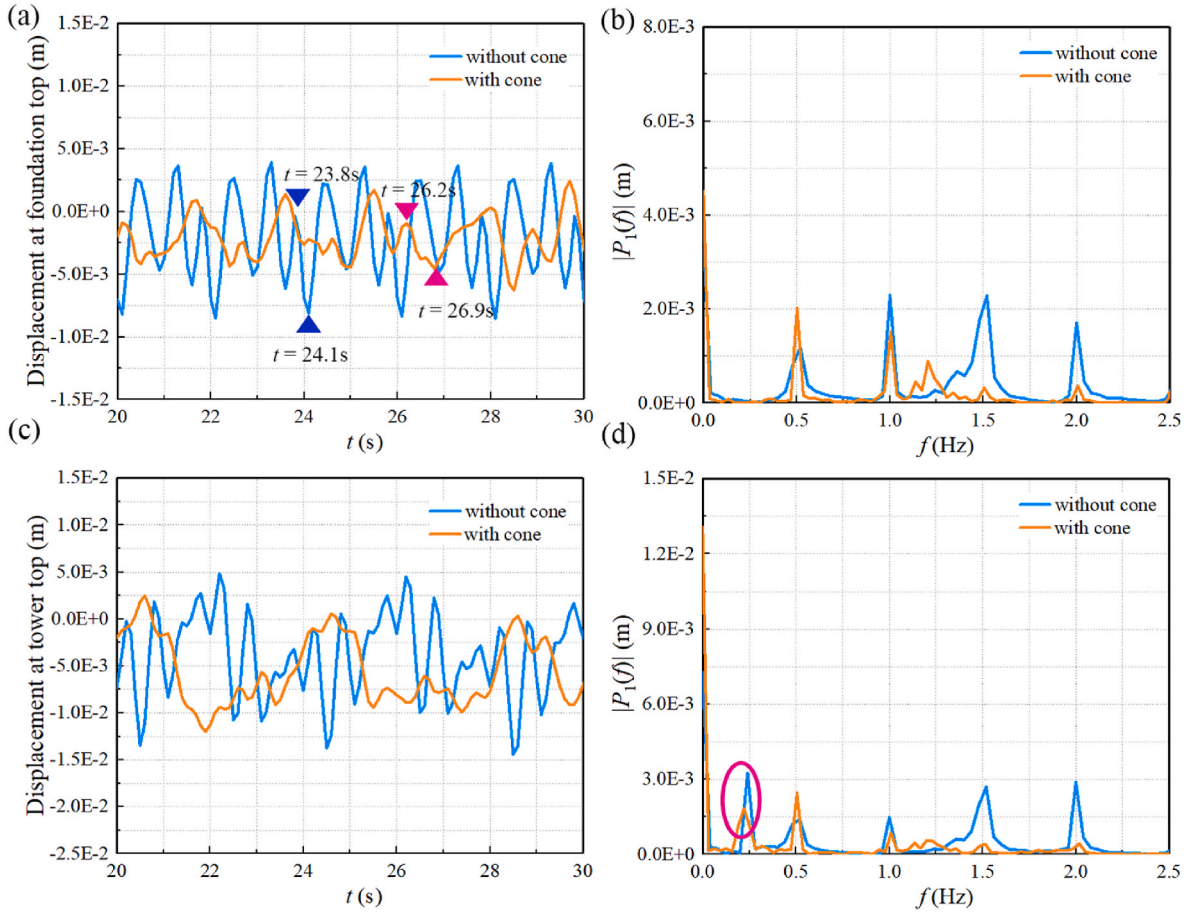

Fig. 8. Time histories and frequency spectra of structure displacement for the "with cone" and "without cone" cases. (a) time series of displacement at foundation top; (b) frequency spectrum of displacement at foundation top; (c) time series of displacement at tower top; (d) frequency spectrum of displacement at tower top.

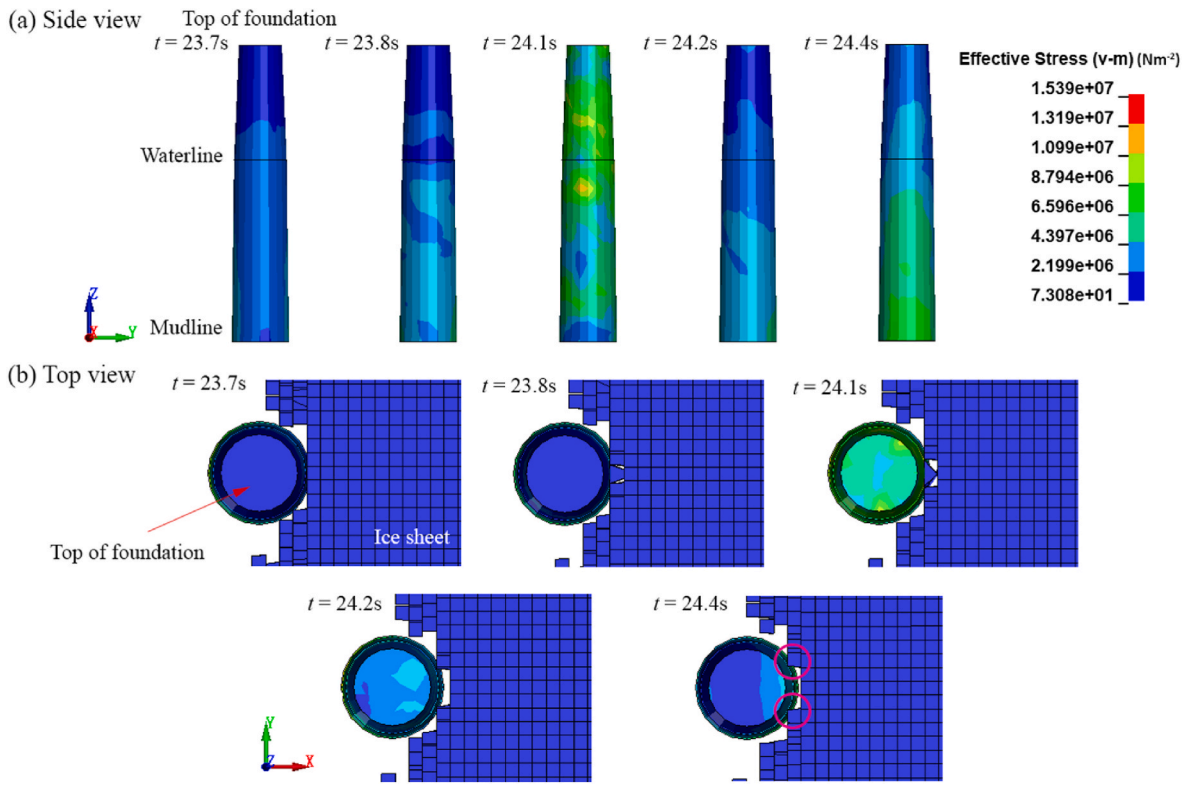

Fig. 9. Von Mises effective stress field distribution in the OWT foundation for the "without cone" case at different time instants.

peak value at approximately 4.4 MPa, while the ice force attains its peak value (Fig. 7(a), marked by a blue triangle). The ice sheet exhibits elastic behavior before it quickly reaches the yield state. During this phase, the ice sheet remains in contact with the OWT, and the OWT moves in the same direction as the ice sheet (negative x direction), generating a small peak in the displacement curve (Fig. 8(a), marked by a blue triangle). The foundation's displacement exhibits a decreasing (negative increasing) trend during the loading phase. The external ice action and the internal force of the OWT are in a static balance when the stress reach the maximum values at $t = 24.1$ s (Fig. 7(a), marked by a blue triangle, and Fig. 9). The crack generates and develops, presenting a softening behavior. Consequently, the ice force on the OWT rapidly decreases (Fig. 7(a)). At $t = 24.2$ s, a brittle crushing failure occurs at the ice edge due to the head-on collision. As the oncoming ice sheet is broken by the OWT, ice fragment detaches from the sheet and the effective stress at the waterline of the foundation diminishes to approximately 2.2 MPa.

It's worth noting that due to the lower ice breaking frequency compared to the structural natural frequency, the OWT's vibration slightly lags behind the changes in the driving force. Consequently, the maximum negative displacement at the foundation top is achieved at approximately $t = 24.1$ s (Fig. 8(a), marked by a blue triangle). As the ice rubbles are cleared after the peak ice action, relaxation vibrations and a decay process ensue in the OWT during the unloading and clearing period, primarily influenced by damping effects from the soil and structure. Given that the natural period of global bending (1/1.332 Hz = 0.75 s) is considerably shorter than the ice action period (2s), the OWT foundation undergoes free vibration cycles before the next ice fragment collides with the OWT at around $t = 25.8$ s. Notably, at $t = 24.4$ s, a small peak in the ice force is observed (Fig. 7(a)), and the effective stress on the OWT foundation at the waterline increases to approximately 4.4 MPa. This increase can be attributed to interactions with side ice edges (marked by red circles). However, due to the reduced contact area with the side ice fragments, the ice force amplitude remains considerably lower than its maximum value. After that, the ice sheet completely detaches from the OWT, marking the beginning of the next periodic cycle.

Akin to the analysis of the "without cone" scenario, the dynamic response characteristics of the OWT with the conical structure during an ice action period from 25.8 s to 26.9 s is investigated. At $t = 25.8$ s, the ice sheet is separated from the OWT, resulting in minimal ice force and effective stress (Figs. 7(a) and Fig. 10). Concurrently, the OWT reaches its maximum positive displacement. Advancing to $t = 26.2$s, as the ice sheet drifts, a set of side ice elements approaches the OWT (marked by red circles in Fig. 10). The effective stress area beyond 0.89 MPa (the light blue and green area) is extended, leading to a gradual increase in the ice force (Fig. 7(a), marked by a red triangle). The OWT moves in the same direction as the oncoming ice sheet, and the displacement of the foundation exhibits a continuous decrease (in the negative x direction), with a notable fluctuation at $t = 26.2$s (Fig. 8(a), marked by a red triangle), coinciding with the time of ice-OWT collision. As the ice sheet continues its advance at $t = 26.5$ s, the closer side ice elements collide with the OWT (marked by yellow circles in Fig. 10), causing the contact area to progressively increase. This results in a further increase in effective stress on the OWT, peaking at approximately $t = 26.8$s, when the leading edge of the ice sheet experiences a head-on collision with the OWT. This moment marks the maximum contact area between the ice sheet and the OWT, initiating the failure of the ice and the clearing of ice fragments around the upward-breaking conical structure, and the effective stress on the cone of the OWT reaches its maximum value of around 6.2 MPa. Subsequently, the ice force reaches its peak (Fig. 7(a), marked by a red triangle), followed by a sudden drop attributed to the separation of ice fragments from the ice sheet. Due to the lag in vibration response of the OWT concerning changes in the driving force, the maximum negative displacement at the foundation top is achieved around $t = 26.9$s (Fig. 8(a), marked by a red triangle). The ice force and effective stress continuously decrease until the ice sheet fully detaches from the OWT. During this phase, the OWT moves in the opposite direction relative to the ice sheet, experiencing free decay during unloading. Consequently, the displacement continues to increase until

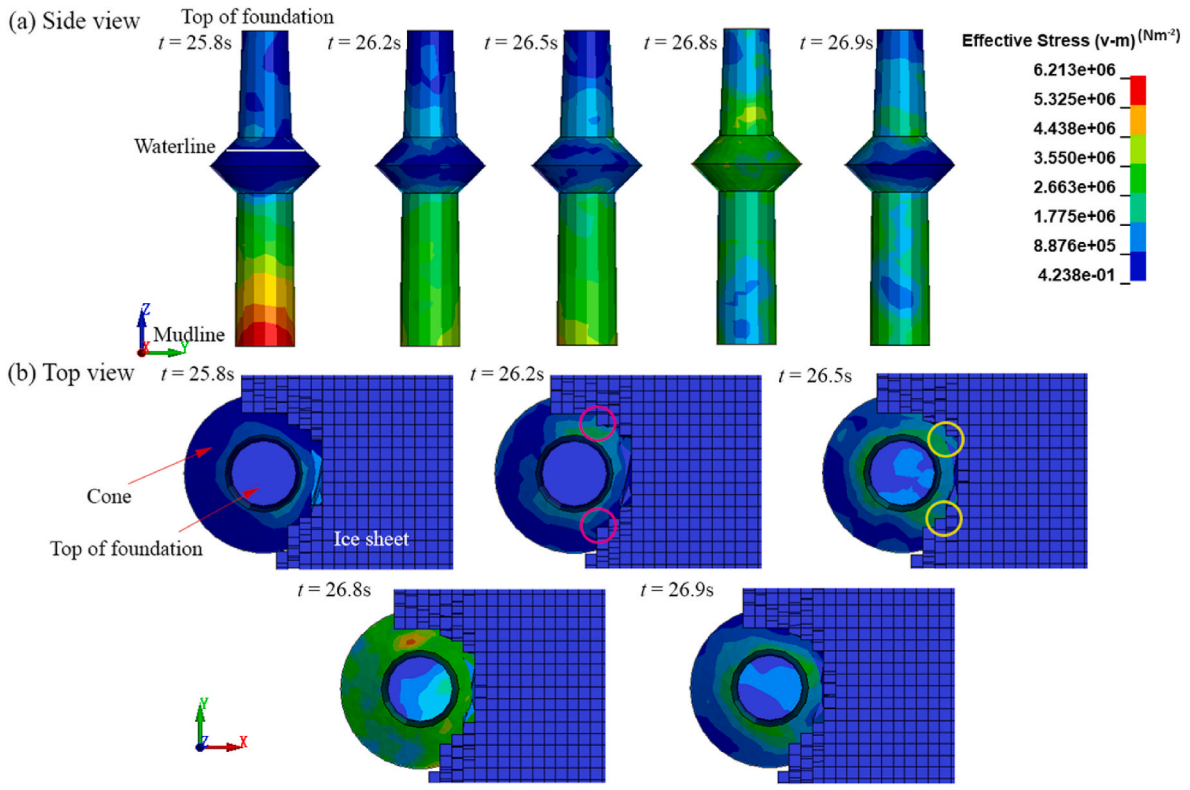

Fig. 10. Von Mises effective stress field distribution in the OWT foundation for the "with cone" case at different time instants.

the commencement of the subsequent periodic cycle.

4.3. *Effects of ice loading position*

In order to elucidate the impact of ice loading position on the dynamics of the OWT structure and the ISSI, a comparison of ice actions and displacements at both the tower and foundation of the OWT varying ice sheet elevations is conducted (Base case, Case2, and Case3). This effectively investigates the loading and response of the OWT at various lake surface water levels.

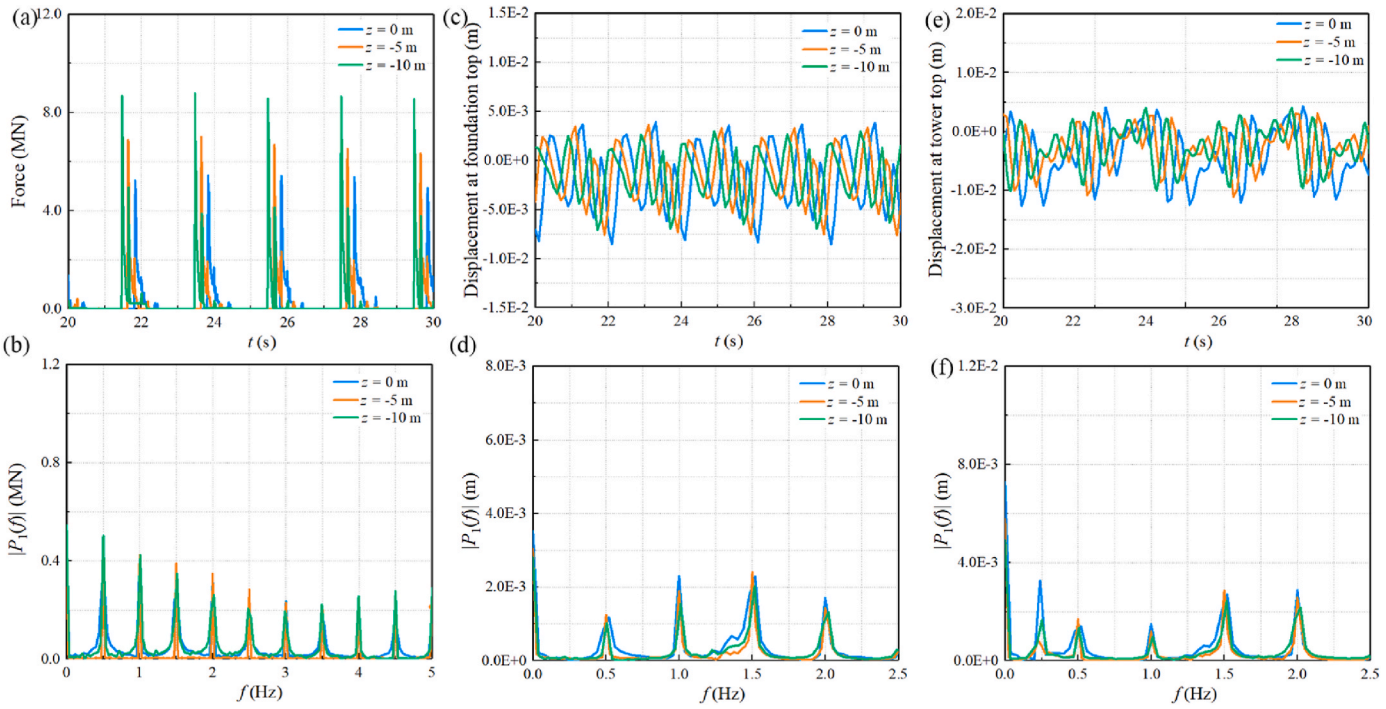

Fig. 11. Time histories and frequency spectra of ice force and structure displacement for different ice loading heights. (a) time series of ice force; (b) frequency spectrum of ice force; (c) time series of displacement at foundation top; (d) frequency spectrum of displacement at foundation top; (e) time series of displacement at tower top; (f) frequency spectrum of displacement at tower top.

Fig. 11(a) displays the ice forces acting on the OWT under different ice loading positions. It's evident that the ice force increases as the ice sheet elevation decreases. The peak ice forces for $z = 0$ m, -5 m, and -10 m are 8.7 MN, 6.9 MN, and 5.2 MN, respectively. This phenomenon arises from the tapered shape of the foundation, which leads to an increase in diameter, and hence, an increase in ice force (Eq. (2) and (3)). Furthermore, the ice force frequency spectrum in Fig. 11(b) reveals peak frequencies corresponding to the ice breaking frequency and its higher harmonics. The peak frequency amplitude exhibits a gradual decrease as the frequency increases, with a slight increase noted at higher frequencies.

The horizontal displacements in the x direction at both the top of the OWT foundation and the tower are compared under different ice acting heights (Fig. 11(c) and (e)). The maximum displacement amplitudes at the foundation top are 0.0133 m, 0.011 m, and 0.009 m for ice loading heights of $z = 0$ m, -5 m, and -10 m, respectively. Similarly, at the tower top, the maximum displacement amplitudes are 0.018 m, 0.015 m, and 0.013 m for the same respective ice loading heights. These show a consistent trend that the displacement amplitudes for both the foundation and tower decrease as the ice loading height decreases. This behavior can be attributed to the simplified representation of the ice-OWT-soil system as a cantilever beam model with a fixed end. Here, the tilting moment generated by lateral ice loading is directly proportional to the ice loading height. Consequently, a decrease in the ice loading height results in a reduced corresponding tilting moment and, consequently, a decrease in horizontal displacement. It also shows that the maximum displacement at the tower is much larger than that at the foundation.

The displacement frequency spectra of the foundation and tower are depicted through FFT analysis (Fig. 11(d) and (f)). For the displacement at the foundation top, the peak frequencies occur at integral multiples of 0.5 Hz, aligning with the ice breaking frequency and its higher harmonics. Interestingly, the spectral amplitude at $f = 1.0$ Hz and 1.5 Hz consistently exhibits the highest values across all cases. In contrast, the displacement at the tower top presents an additional peak frequency at $f = 0.25$ Hz, which corresponds to the first bending mode of the tower. This observation signifies that the dynamics of the tower are more intricate, influenced not only by the ice-induced vibrations but also by its inherent structural modes. At $z = 0$ m, the highest spectral amplitude is at $f = 0.25$ Hz. In contrast, for $z =$ -5 m and $z = -10$ m, the highest spectral amplitude is at $f = 1.5$ Hz. This indicates that as the ice loading height approaches the tower, the natural frequency of the tower becomes the dominant factor influencing structure's vibration.

4.4. Effects of glacial soil properties

To illuminate the influence of soil properties on the dynamics of the OWT structure and the ISSI, the ice actions and displacements at both the tower and foundation of the OWT in the x direction are examined with different soil shear moduli (Base case, Case4, and Case5), cohesions (Base case, Case6, and Case7) and angles of friction (Base case, Case8, and Case9), respectively.

4.4.1. Effects of shear modulus

Fig. 12 presents the ice force and displacements time histories at both the tower and foundation top of the OWT under different shear moduli in glacial soils. It shows that the ice force is not significantly affected by variations of elastic shear modulus. However, slightly higher ice force peaks of the 1.0G case than 1.5G case are observed. In the force frequency spectrum (Fig. 12(b)), it is discerned that peak frequencies align with integer multiples of 0.5 Hz, coinciding with the ice breaking frequency and its higher harmonics. This consistency is attributed to equal ice mesh size, ice thickness, and ice drift speed. Interestingly, the fundamental ice breaking frequency and its odd multiple harmonics exhibit a broader frequency span and a flatter shape compared to the even multiple harmonics, which display sharper and narrower peaks.

Concerning the displacement at the foundation top (Fig. 12(c)), the maximum amplitude of the displacement is 0.011 m, 0.013 m, and 0.015 m for shear modulus of 0.5G, 1.0G and 1.5G, respectively. This observation underscores that the maximum displacement at the foundation top increases with higher elastic shear modulus. This phenomenon can be elucidated by considering the distribution of effective plastic

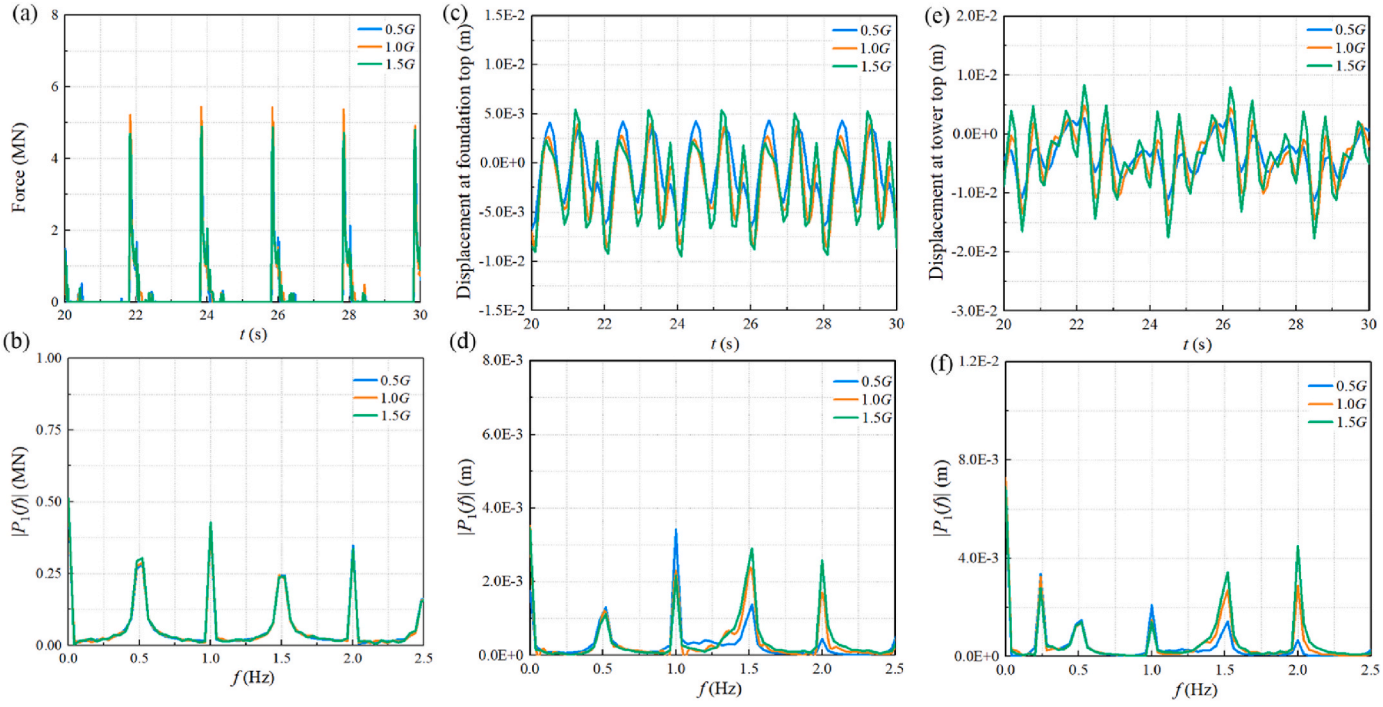

Fig. 12. Time histories and frequency spectra of ice force and structure displacement for different soil shear moduli. (a) time series of ice force; (b) frequency spectrum of ice force; (c) time series of displacement at foundation top; (d) frequency spectrum of displacement at foundation top; (e) time series of displacement at tower top; (f) frequency spectrum of displacement at tower top.

strain within the soil.

As the ice cover approaches the OWT, the OWT foundation initiates soil compression, leading to a localized elevation in soil pressure on the windward side. During the subsequent unloading stage, characterized by the separation of ice fragments from the ice sheet, the OWT structure undergoes free decay vibration. This vibration results in an augmented soil pressure on the opposite side. Upon reaching a critical displacement of the OWT foundation, specific areas of the soil attain the failure yield criterion, as manifested by the field of effective plastic strain, forming a slip surface. Effective plastic strain is a monotonically increasing scalar value that represents the plastic deviatoric component of the rate of deformation tensor. Fig. 13 illustrates the effective plastic strain of the soil at the same time instant ($t = 20$s).

It reveals that the effective plastic strain in the soil escalates as the shear modulus increases. The maximum effective plastic strain records values of 0.024, 0.035, and 0.049 for shear modulus of 0.5G, 1.0G and 1.5G, respectively. Given the same yield strength (i.e., with the same cohesion and friction angle), an increase in shear modulus results in a decrease in yield strain. Consequently, this decrease in yield strain leads to an earlier transition into the plastic deformation regime, culminating in a greater degree of plasticity, and hence, larger structural displacements. The soil primarily demonstrates an elastic response, but in the vicinity of the OWT foundation, it approaches the shear strength threshold as defined by the Mohr-Coulomb criterion, exhibiting localized yielding at a limited number of points. The slip surface exhibits a generally symmetric and approximately circular configuration. To clearly depict the slip surface in the soil, the cross-section of the plastic strain contour is presented in the X-Z plane in Fig. 13 (e ~ f). Notably, in cases with a small shear modulus, the diameter of the slip surface is observed to be larger compared to large shear modulus cases.

In the frequency spectrum of displacement at the foundation top (Fig. 12(d)), the highest spectral amplitude occurs at $f = 1.0$ Hz for a shear modulus of 0.5G. However, for the 1.0G and 1.5G cases, the peak shifts to $f = 1.5$ Hz, indicating that the vibration of the foundation is notably sensitive to soil properties and external forces. As the shear modulus increases, the peak vibration frequency with the highest spectrum amplitude tends to elevate. Given that natural frequency of soil profile is proportional to the shear wave velocity, and the shear modulus exhibits a direct relationship with the square of the shear wave velocity. It follows that an augmentation in shear modulus corresponds to an escalation in the natural frequency of the soil profile. In instances characterized by greater shear modulus values, the influence of higher ice breaking harmonics becomes more pronounced in dictating the vibrational behavior of the OWT foundation. This phenomenon parallels the observations in the ice force spectrum, where the peak frequencies at 0.5 Hz and 1.5 Hz manifest a broader and more even spectral shape in contrast to those at 1.0 Hz and 2.0 Hz. Examining the displacement at the tower top (Fig. 12(e)), the maximum amplitude measures 0.014 m, 0.018 m, and 0.026 m for shear modulus of 0.5G, 1.0G and 1.5G, respectively. The displacement amplitude increases with increasing shear modulus. Due to the constraints imposed by the soil, the deflection of the OWT at the foundation is smaller than at the tower top.

In the displacement frequency spectrum at the tower top (Fig. 12(f)), the maximum spectrum amplitude occurs at approximately $f = 0.25$ Hz for the 0.5G and 1.0G cases, corresponding to the afore-aft (F-A) bending mode of the tower. However, for the 1.5G case, this shifts to $f = 2.0$ Hz, indicating that the vibration characteristics of the tower are primarily influenced by the natural frequency of the tower in cases of low shear modulus. In contrast, in scenarios of high shear modulus, the higher harmonics of ice breaking frequency play a more pivotal role.

4.4.2. *Effects of cohesion*

Fig. 14 illustrates the influences of cohesions in glacial soils on ice force and displacements at both the tower and foundation top of the OWT. Notably, there's no significant variation in ice force observed with changing cohesions. This suggests that the cohesion of glacier soils may

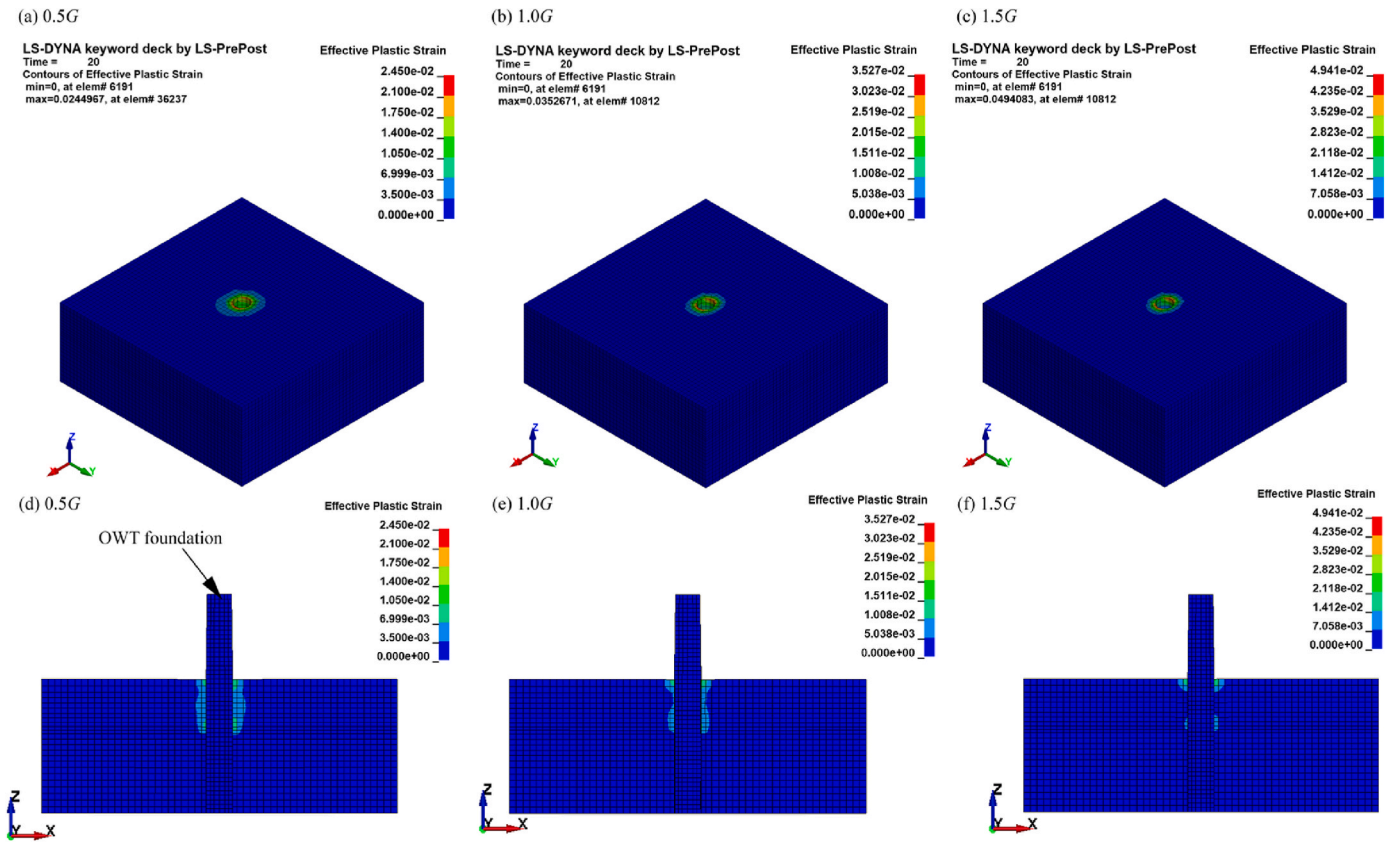

Fig. 13. Plastic strain distribution in soils with various shear moduli at $t = 20$ s.

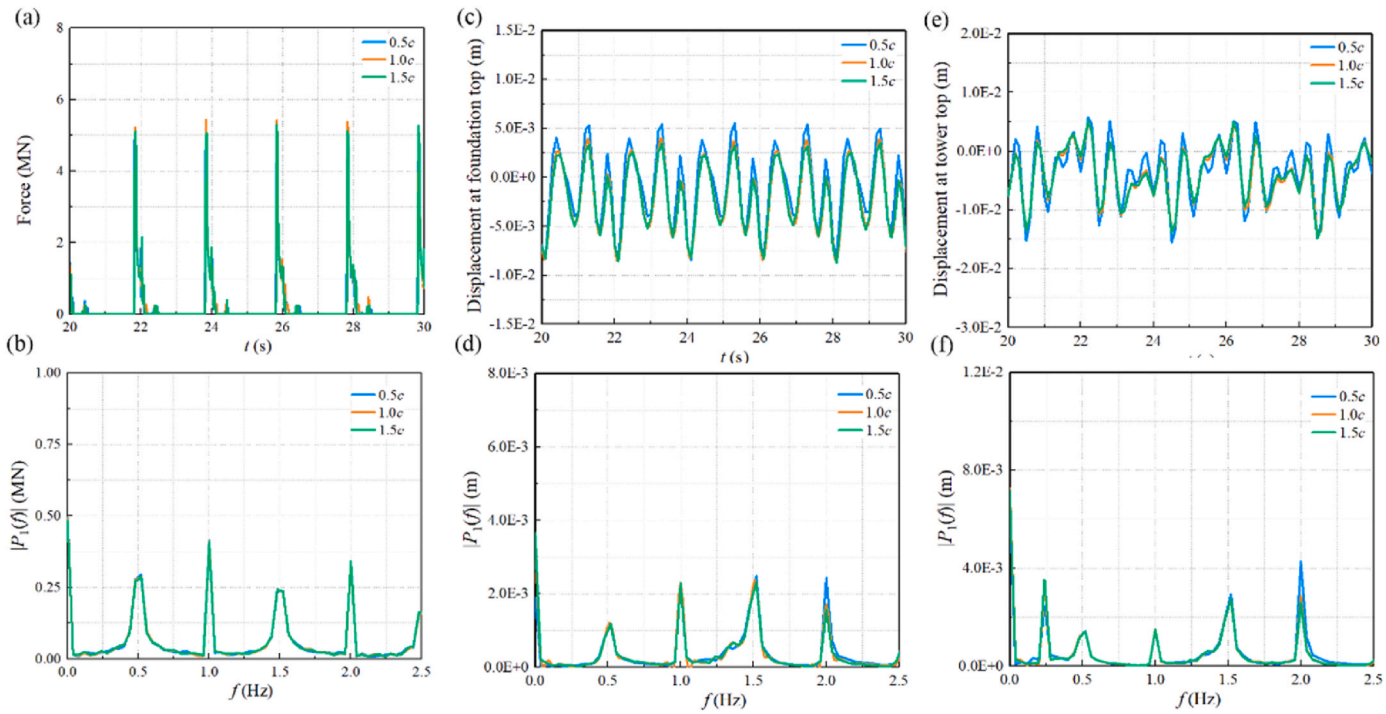

Fig. 14. Time histories and frequency spectra of ice force and structure displacement for different soil cohesions. (a) time series of ice force; (b) frequency spectrum of ice force; (c) time series of displacement at foundation top; (d) frequency spectrum of displacement at foundation top; (e) time series of displacement at tower top; (f) frequency spectrum of displacement at tower top.

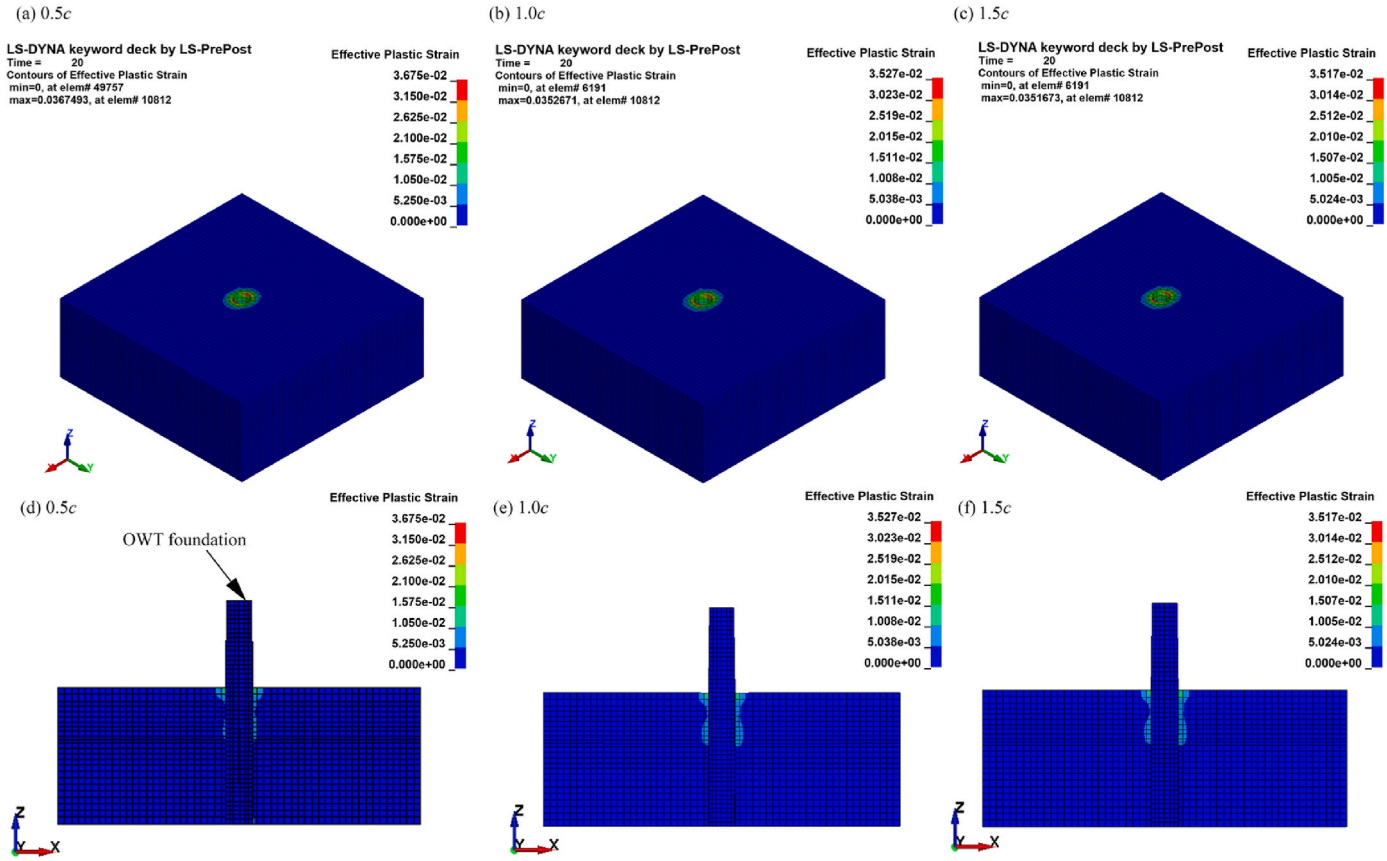

Fig. 15. Plastic strain distribution in soils with various cohesions at $t = 20$ s.

not be a critical factor affecting ice force. In the force frequency spectrum (Fig. 14(b)), peak frequencies align with integer multiples of 0.5 Hz, coinciding with the ice breaking frequency and its higher harmonics. For the displacement at the foundation top (Fig. 14(c)), the maximum amplitude of the displacement is 0.014 m, 0.013 m, and 0.012 m for cohesion of 0.5*c*, 1.0*c* and 1.5*c*, respectively. It shows that the maximum displacement amplitude at the foundation top generally decreases with increasing cohesion. This phenomenon is in line with Eq. (1), where the reduction in cohesion leads to a decrease in the shear strength of the glacial soil. Consequently, weakened soil resistance induces an increase in structural dynamic response. As depicted in Fig. 15, the maximum effective plastic strain for cohesions of 0.5*c*, 1.0*c* and 1.5*c* are 0.037, 0.035, and 0.035, respectively. The maximum effective plastic strain decreases with increasing cohesion, though the distinctions among the cases remain relatively inconsequential, and the diameter of the slip surface is noted to be generally consistent across different cohesion values (Fig. 15(e ~ f)). In the frequency spectrum of displacement at the foundation top (Fig. 14(d)), the maximum spectral amplitude is observed at $f = 1.5$ Hz for all the cases, and a broad frequency span around $f = 1.5$ Hz is observed. Furthermore, an equivalent highest spectral amplitude can be observed at $f = 2.0$ Hz for the 0.5c case. For the displacement at the tower top (Fig. 14(e)), the maximum amplitude is 0.021 m, 0.018 m, and 0.018 m for cohesions of 0.5*c*, 1.0*c*, and 1.5*c*, respectively. The displacement amplitude of the tower top increases with decreasing cohesion but no discernible difference between the conditions of 1.0*c* and 1.5*c* is observed. In the displacement frequency spectrum at the tower top (Fig. 14(f)), the maximum spectral amplitude occurs at approximately $f = 0.25$ Hz and 2.0 Hz for the 1.5*c* and 0.5*c*, respectively. Similar to the impacts of shear modulus, the dynamic ice breaking force assumes a more pivotal role in low cohesion conditions.

4.4.3. *Effects of friction angle*

In Fig. 16, the ice forces and displacements in the *x* direction at both the tower and foundation top of the OWT under different friction angles are presented. Similar to the effects of cohesion, no significant variation in ice force with varying friction angles is observed. This suggests that the angle of friction of glacier soils is not a dominant factor affecting ice force. Again, in the force frequency spectrum (Fig. 16(b)), peak frequencies align with integer multiples of 0.5 Hz, in line with the ice breaking frequency and its higher harmonics.

For the structural displacement at the foundation top (Fig. 16(c)), the maximum amplitude of displacement is 0.013 m, 0.013 m, and 0.012 m for friction angles of 0.8tanφ, 1.0tanφ, and 1.2tanφ, respectively. This trend indicates that displacement at the foundation top generally increases with decreasing friction angle but the difference is minor. This can also be interpreted by Eq. (1), as the reduction in tanφ leads to a weakening of the shear strength of glacial soil. As shown in Fig. 17, the maximum effective plastic strain for friction angles of 0.8tanφ, 1.0tanφ, and 1.2tanφ are 0.047, 0.035, and 0.032, respectively. The diameter of the slip surface shows minimal variation across different friction angles, as depicted in Fig. 17(e ~ f). However, the OWT dynamic response is not significantly affected by friction angle (or tanφ) because the soil has a predominantly elastic soil response in these conditions. The maximum effective plastic strain decreases with escalating internal friction angle. In the frequency spectrum (Fig. 16(d)), the maximum spectrum amplitude for all cases occurs at $f = 1.5$ Hz, emphasizing the sensitivity of foundation vibration to the nature of external forces, particularly ice loading.

For the displacement at the tower top (Fig. 16(e)), the friction angle of the soil has minimal effect on the tower's displacement. The maximum amplitudes are all around 0.018 m for the three friction angles. The differences are subtle among cases. In the displacement frequency spectrum at the tower top (Fig. 16(f)), different to the spectrum at the foundation top, the highest spectrum amplitude occurs at around $f = 0.25$ Hz, corresponding to the F-A bending mode of the tower. This finding underscores that the vibration behavior of the tower is significantly influenced by self-restoring forces.

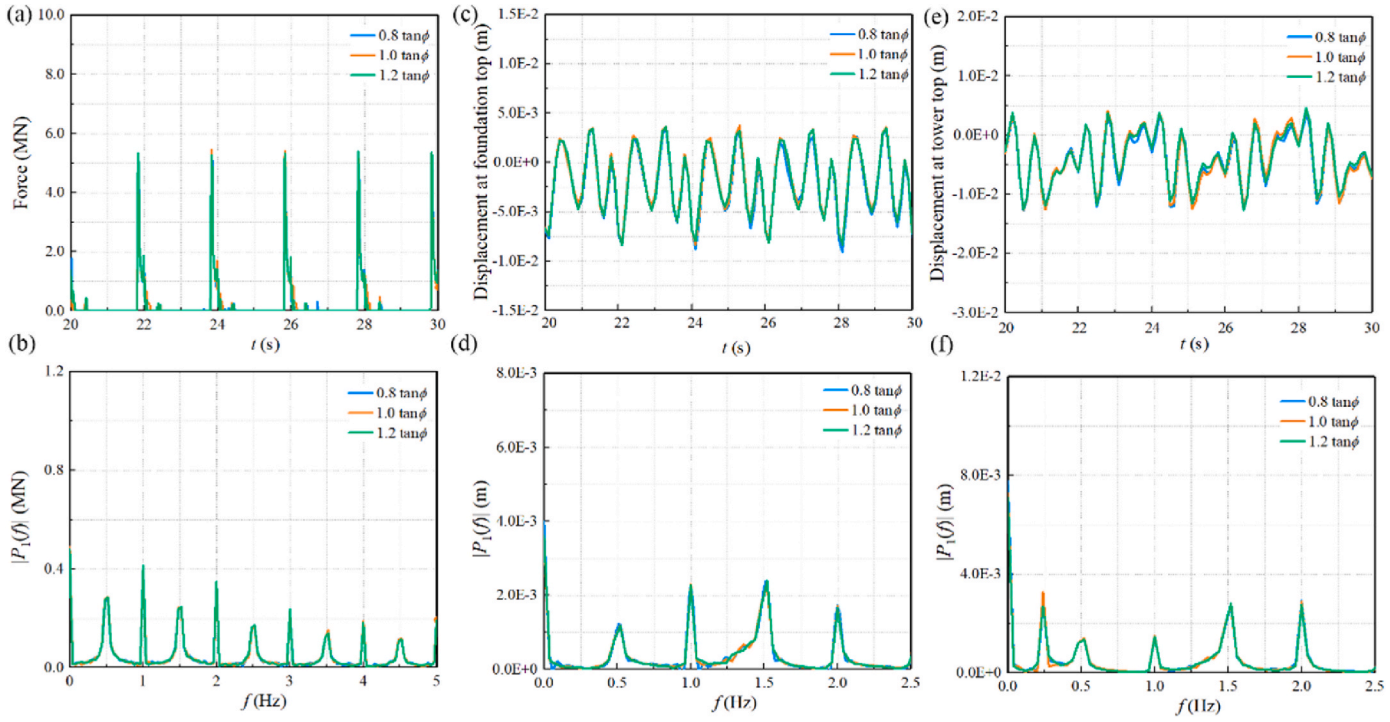

Fig. 16. Time histories and frequency spectra of ice force and structure displacement for different soil angles of friction. (a) time series of ice force; (b) frequency spectrum of ice force; (c) time series of displacement at foundation top; (d) frequency spectrum of displacement at foundation top; (e) time series of displacement at tower top; (f) frequency spectrum of displacement at tower top.

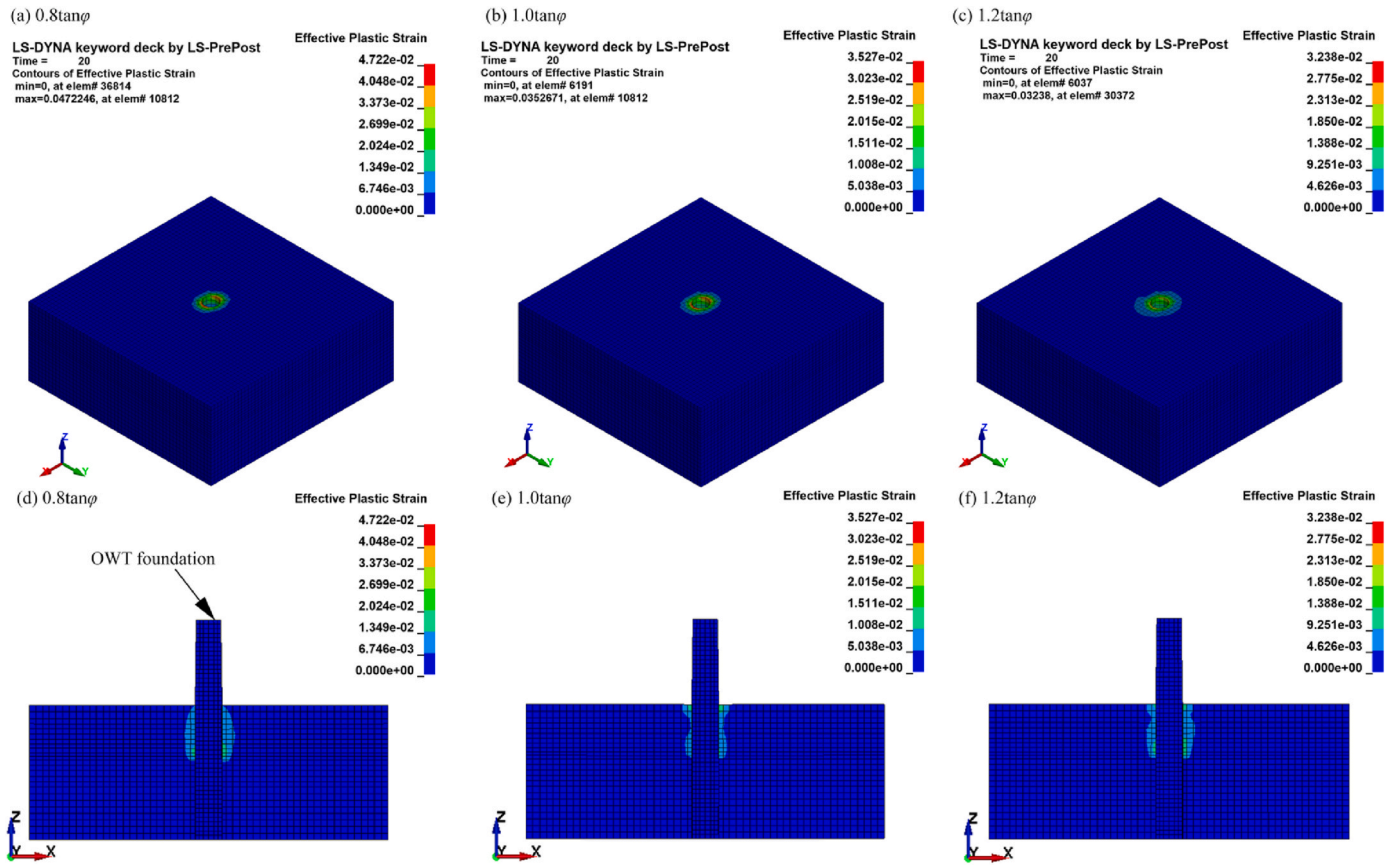

Fig. 17. Plastic strain distribution in soils with various friction angles at $t = 20$ s.

5. Conclusion

This study aims to offer a systematic investigation of the complex interactions within the ice-OWT-soil system, shedding light on critical aspects that are vital for the design, operation, and safety of OWTs in regions characterized by glacial soils, such as the Great Lakes. Therefore, a three-dimensional coupled ice-structure-soil interaction numerical model is developed for dynamic response analysis. The coupled CEM-FEM is adopted for ice load simulation. The soil-structure interaction is calculated using the Mohr-Coulomb model for glacial soils. An offshore wind case study proposed in Lake Erie is selected for offshore wind turbine dynamic analysis. The simulated ice forces and structural deflections are validated against theoretical and experimental data. A parametric study of the influence of conical structures, ice loading location, and soil properties on the ISSI are investigated. The main conclusions are briefly summarized as follows.

(1) The addition of conical structures significantly reduces horizontal ice forces on offshore wind turbines, enhancing structural stability. The conical shape leads to longer ice action periods, affecting loading and unloading cycles. The OWT with a conical structure exhibits smaller displacement in comparison to the vertical-sided case. However, the effects of the cone are more localized at the elevation where ice collides with the OWT. In addition, higher-frequency components play a significant role in the displacement of the "without cone" case.

(2) The dynamics of the tower are more intricate compared to that at the foundation top, influenced not only by the ice-induced vibrations but also by its inherent structural modes. Due to the superimposed tower natural period vibrations, the time history of the displacement exhibits more irregular patterns.

(3) Lower ice loading positions result in increased peak ice force and reduced structural displacements at both the foundation and tower top. As the ice loading elevation approaches the tower, the dominant factor affecting the vibration of the structure shifts from dynamic ice loads to the natural frequencies of the tower.

(4) The analysis reveals that the elastic shear modulus of glacial soils impacts the dynamics of the OWT structure, especially in terms of displacements. The vibration characteristics of the tower exhibit a predominance reliance on the natural frequencies in cases with low shear modulus of glacial soils. In contrast, higher harmonics of ice-breaking frequencies highlight the increased significance with high shear modulus cases.

(5) Decreased cohesion and lower friction angles lead to increased structural displacements. However, glacier soil strength properties (cohesion and tanφ) are not a dominant factor affecting ice force and structure dynamic response and structure dynamic response in a predominantly elastic soil response scenario.

These findings provide insights for OWT engineers, guiding the design of structures that can withstand the dynamic forces in icy offshore environments. Careful consideration of conical structures, ice loading positions, and soil properties is essential for OWT resilience and long-term performance. However, it is imperative to acknowledge that this model does not take into account phenomena such as strain softening and the development of excess pore pressure in the soil. Furthermore, the Mohr- Coulomb model, as a simple elastic-perfectly plastic model, is limited due to its inability to capture the nonlinear decrease in shear modulus with increasing shear strain. These aspects will be investigated in follow-on research.

CRediT authorship contribution statement

Pengxu Zou: Writing – original draft, Visualization, Validation, Software, Methodology, Investigation, Formal analysis, Data curation, Conceptualization. **Jeremy D. Bricker:** Writing – review & editing, Supervision, Funding acquisition, Conceptualization. **Ayumi Fujisaki-Manome:** Writing – review & editing, Supervision, Funding acquisition. **Fernando E. Garcia:** Writing – review & editing, Supervision, Formal analysis.

Declaration of competing interest

The authors declare that they have no known competing financial interests or personal relationships that could have appeared to influence the work reported in this paper.

Data availability

Data will be made available on request.

Acknowledgement

The study presented in this paper was funded by the Cooperative Institute for Great Lakes Research (CIGLR) postdoctoral fellowship.

References

Araz, O., 2022. Optimization of tuned mass damper inerter for a high-rise building considering soil-structure interaction. Arch. Appl. Mech. 92 (10), 2951–2971.
Araz, O., Farsangi, E.N., 2023. Optimum tuned tandem mass dampers for suppressing seismic-induced vibrations considering soil-structure interaction. In: Structures, pp. 1146–1159.
Araz, O., Elias, S., Kablan, F., 2023. Seismic-induced vibration control of a multi-story building with double tuned mass dampers considering soil-structure interaction. Soil Dynam. Earthq. Eng. 166, 107765.
Beik, O., Al-Adsani, A., 2020. Wind turbine productivity and wind energy assessment: an ontario case study. In: 2020 IEEE Electric Power and Energy Conference, EPEC. https://doi.org/10.1109/EPEC48502.2020.9320110.
Chung, C.K., Finno, R.J., 1992. Influence of depositional processes on the geotechnical parameters of Chicago glacial clays. Eng. Geol. 32 (4) https://doi.org/10.1016/0013-7952(92)90050-9.
Clarke, B.G., 2017. Engineering of Glacial Deposits. https://doi.org/10.1201/9781315149356.
Di, S., Xue, Y., Wang, Q., Bai, X., 2017. Discrete element simulation of ice loads on narrow conical structures. Ocean Eng. 146 https://doi.org/10.1016/j.oceaneng.2017.09.033.
Gaur, S., Elias, S., Höbbel, T., Matsagar, V.A., Thiele, K., 2020. Tuned mass dampers in wind response control of wind turbine with soil-structure interaction. Soil Dynam. Earthq. Eng. 132, 106071.
Gholipour, G., Zhang, C., Li, M., 2018. Effects of soil–pile interaction on the response of bridge pier to barge collision using energy distribution method. Struct. Infrastruct. Eng. 14 (11) https://doi.org/10.1080/15732479.2018.1450427.
Gürtner, A., Konuk, I., Løset, S., 2008. A computational cohesive element model for the simulation of ice drift on arrangements of ice protection piles. Comput. Struct. 131–141.
Gürtner, A., Bjerkås, M., Forsberg, J., Hilding, D., 2010. Numerical modelling of a full scale ice event. In: 20th IAHR International Symposium on Ice. Lahti, Finland: IAHR, pp. 77–88.
Hammer, T.C., Willems, T., Hendrikse, H., 2023. Dynamic ice loads for offshore wind support structure design. Mar. Struct. 87 https://doi.org/10.1016/j.marstruc.2022.103335.
Hendrikse, H., Metrikine, A., 2016. Edge indentation of ice with a displacement-controlled oscillating cylindrical structure. Cold Reg. Sci. Technol. 121 https://doi.org/10.1016/j.coldregions.2015.10.013.
Hilding, D., Forsberg, J., Gürtner, A., 2011. Simulation of ice action loads on offshore structures. In: Proceedings of the 8th European LS-DYNA Users Conference, Strasbourg.
Ismael, N.F., 1998. Lateral loading tests on bored piles in cemented sands. In: Deep Foundations on Bored and Auger Piles. https://doi.org/10.1201/9781003078517-17.
ISO 19906, 2019. Petroleum and Natural Gas Industries - Arctic Offshore Structures.
Jayasinghe, L.B., Waldmann, D., Shang, J., 2020. Impact of pile punching on adjacent piles: insights from a 3D coupled SPH-FEM analysis. Appl. Mech. 1 (1) https://doi.org/10.3390/applmech1010004.
Kavitha, P.E., Beena, K.S., Narayanan, K.P., 2016. A review on soil–structure interaction analysis of laterally loaded piles. Innovative Infrastructure Solutions 1 (1). https://doi.org/10.1007/s41062-016-0015-x.
Konuk, I., Gürtner, A., Yu, S., 2009a. A cohesive element framework for dynamic ice-structure interaction problems - Part I: review and formulation. In: Proceedings of the International Conference on Offshore Mechanics and Arctic Engineering - OMAE. https://doi.org/10.1115/OMAE2009-79262.
Konuk, I., Gürtner, A., Yu, S., 2009b. A cohesive element framework for dynamic ice-structure interaction problems - Part II: implementation. In: Proceedings of the International Conference on Offshore Mechanics and Arctic Engineering - OMAE. https://doi.org/10.1115/OMAE2009-80250.
Leppäranta, M., 2011. The Drift of Sea Ice. Springer Science & Business Media.
ling Zhang, X., Zhou, R., liang Zhang, G., Han, Y., 2023. A corrected p-y curve model for large-diameter pile foundation of offshore wind turbine. Ocean Eng. 273 https://doi.org/10.1016/j.oceaneng.2023.114012.
Liu, Y., et al., 2023. Investigation on the interaction between ice and monopile offshore wind turbine using a coupled CEM–FEM model. Ocean Eng. 281 https://doi.org/10.1016/j.oceaneng.2023.114783.
Long, X., Liu, S., Ji, S., 2020. Discrete element modelling of relationship between ice breaking length and ice load on conical structure. Ocean Eng. 201 https://doi.org/10.1016/j.oceaneng.2020.107152.
Lu, W., Lubbad, R., Løset, S., 2014. Simulating ice-sloping structure interactions with the cohesive element method. J. Offshore Mech. Arctic Eng. 136 (3) https://doi.org/10.1115/1.4026959.
Mickelson, D.M., Edil, T.B., Guy, D.E., 2004. Erosion of Coastal Bluffs in the Great Lakes, vol. 1693. US Geol. Surv. Prof. Pap.
Mokhtar, A.S.A., Abdel-Motaal, M.A., Wahidy, M.M., 2014. Lateral displacement and pile instability due to soil liquefaction using numerical model. Ain Shams Eng. J. 5 (4) https://doi.org/10.1016/j.asej.2014.05.002.
Moreau, L., et al., 2020. Sea ice thickness and elastic properties from the analysis of multimodal guided wave propagation measured with a passive seismic array. J. Geophys. Res. Ocean. 125 (4) e2019JC015709.
Nord, T.S., Lourens, E.M., Määttänen, M., Øiseth, O., Høyland, K.V., 2015. Laboratory experiments to study ice-induced vibrations of scaled model structures during their interaction with level ice at different ice velocities. Cold Reg. Sci. Technol. 119 https://doi.org/10.1016/j.coldregions.2015.06.017.
Rodriguez-Galván, E., Álamo, G.M., Medina, C., Maeso, O., 2023. Influence of seabed profile on the seismic response of monopile-supported offshore wind turbines including dynamic soil-structure interaction. Mar. Struct. 92, 103500.
Sand, B., Horrigmoe, G., 1998. Finite element analysis of breaking ice forces on conical structures. New York Ice Surf. waters Proc. 14th Int. Symp. ice 1, 27–31. July 1998.
Shen, H.H., Ackley, S.F., Yuan, Y., 2004. Limiting diameter of pancake ice. J. Geophys. Res. Ocean. 109 (C12).
Sheng, D., Wriggers, P., Sloan, S.W., 2007. Application of frictional contact in geotechnical engineering. Int. J. GeoMech. 7 (3) https://doi.org/10.1061/(asce)1532-3641(2007)7:3(176).
Shi, W., Liu, Y., Wang, W., Cui, L., Li, X., 2023. Numerical study of an ice-offshore wind turbine structure interaction with the pile-soil interaction under stochastic wind loads. Ocean Eng. 273 https://doi.org/10.1016/j.oceaneng.2023.113984.
Skatulla, S., et al., 2022. Physical and mechanical properties of winter first-year ice in the Antarctic marginal ice zone along the Good Hope Line. Cryosphere 16 (7), 2899–2925.
Ushev, E., 2018. Laboratory Investigation of the Mechanical Properties of Cowden till under Static and Cyclic Conditions. Imperial College London.
Wagner, L., Karpinski, D., Nagusky, B., 2018. DE-EE0006714 Final Report-Project IcebreakerTM (No. DOE-LEEDCO-6714-1). Lake Erie Energy Development Corp. (LEEDCo), Cleveland, OH (United States).
Wang, Y., Yao, X., Teo, F.C., Zhang, J., 2020. Cohesive element method to level ice-sloping structure interactions. Int. J. Offshore Polar Eng. 30 (4) https://doi.org/10.17736/ijope.2020.jc787.
Wang, B., Liu, Y., Zhang, J., Shi, W., Li, X., Li, Y., 2022a. Dynamic analysis of offshore wind turbines subjected to the combined wind and ice loads based on the cohesive element method. Front. Mar. Sci. 9, 956032.
Wang, P., Zhao, M., Zhang, B., Xu, H., Du, X., 2022b. Effects of rocking impedance and soil shear stress of the free-field on the dynamic response of an end-bearing pile during horizontal earthquakes. Comput. Geotech. 150 https://doi.org/10.1016/j.compgeo.2022.104919.
Wang, G., Zhang, D., Yue, Q., Yu, S., 2022c. Study on the dynamic ice load of offshore wind turbines with installed ice-breaking cones in cold regions. Energies 15 (9), 3357.
Xing, W., Cong, S., Ling, X., Li, X., Cheng, Z., Tang, L., 2023. Numerical study of ice loads on different interfaces based on cohesive element formulation. Sci. Rep. 13 (1), 14434.
Yang, Y., Bashir, M., Li, C., Wang, J., 2019. Analysis of seismic behaviour of an offshore wind turbine with a flexible foundation. Ocean Eng. 178 https://doi.org/10.1016/j.oceaneng.2019.02.077.
Yuan, B., Chen, M., Chen, W., Luo, Q., Li, H., 2022. Effect of pile-soil relative stiffness on deformation characteristics of the laterally loaded pile. Adv. Mater. Sci. Eng. 2022 https://doi.org/10.1155/2022/4913887.
Zhu, B., Sun, C., Jahangiri, V., 2021. Characterizing and mitigating ice-induced vibration of monopile offshore wind turbines. Ocean Eng. 219 https://doi.org/10.1016/j.oceaneng.2020.108406.
Zou, P.X., Bricker, J.D., Chen, L.Z., Uijttewaal, W.S.J., Simao Ferreira, C., 2022. Response of a submerged floating tunnel subject to flow-induced vibration. Eng. Struct. 253 https://doi.org/10.1016/j.engstruct.2021.113809.
Zou, P.X., Bricker, J.D., Fujisaki-Manome, A., 2023a. Dynamic Response of an Offshore Wind Turbine Subject to Ice Loading in Glacial Soils. Mar. Struct. under review.
Zou, P.X., Ruiter, N., Uijttewaal, W.S.J., Chen, X.X., Peters, D.J., Bricker, J.D., 2023b. Experimental study of surface roughness effects on hydrodynamic characteristics of a

submerged floating tunnel. Appl. Ocean Res. 135 https://doi.org/10.1016/j.apor.2023.103557.